modality for cancer. In particular, radioimmunotherapy in B-cell non-Hodgkin's lymphoma targeting the CD20 antigen, which is found on the B-cell surface, has clearly demonstrated its efficacy [1, 2]. Consequently, ^{90}Y ibritumomab tiuxetan (Zevalin) and ^{131}I tositumomab (Bexxar), both targeting the CD20 antigen, have been approved by the United States Food and Drug Administration for the treatment of refractory or relapsed low-grade, follicular, or transformed B-cell non-Hodgkin's lymphoma [3, 4]. Both radiopharmaceuticals have been shown to produce high response rates, but they also have some shortcomings as radionuclides. ^{131}I emits a high-energy gamma ray, 364 keV, that is not ideal for imaging and exposes patients to unnecessary radiation. Meanwhile, because ^{90}Y is a pure beta emitter, imaging is difficult with ^{90}Y-mAb, and dosimetry should be performed with ^{111}In-mAb before the ^{90}Y-mAb therapy. However, ^{111}In-mAb might not accurately predict the dosimetry of ^{90}Y-mAb because it has been reported that ^{111}In-mAb does not parallel the uptake of ^{86}Y-mAb in bone [5].

Rhenium has two useful radionuclides for radionuclide therapy, ^{186}Re and ^{188}Re. ^{186}Re and ^{188}Re are currently considered to be appropriate candidates for therapeutic applications due to their favorable nuclear properties [6, 7]. Both rhenium radioisotopes decay with the emission of not only beta particles for therapy but also gamma rays, which are suitable for external detection with gamma cameras: ^{186}Re ($t_{1/2}$ = 3.68 days, β^-_{max} = 1.07 MeV, γ = 137 keV) and ^{188}Re ($t_{1/2}$ = 16.98 h, β^-_{max} = 2.12 MeV, γ = 155 keV). In addition, in the case of ^{188}Re, a further advantage in clinical use is that ^{188}Re is conveniently produced from a transportable, in-house alumina-based ^{188}W/^{188}Re generator, similar to a ^{99}Mo/^{99m}Tc generator [8, 9].

Previous reports have demonstrated the usefulness of $^{186/188}$Re radionuclide therapy. However, there are problems when proteins such as antibodies are used as carriers of $^{186/188}$Re. A direct label method is not ideal because of the instability of labeled mAb, especially in the case of ^{186}Re [10]. The mercaptoacetylglycylglycylglycine (MAG3) ligand forms a stable ^{186}Re–MAG3 complex [11]; the usefulness of ^{186}Re–MAG3–mAb has been demonstrated in preclinical studies [12, 13]. However, the labeling method using bifunctional chelating agents such as the N_3S (MAG3) and N_2S_2 (MAMA) ligand requires conjugation with the $^{186/188}$Re complex to mAb after radiolabeling because this radiolabeling procedure requires severe conditions, such as heating and a non-neutral pH [14, 15]. These complicated processes limit the clinical utility of radiolabeled mAb. Thus, we planned the preparation by a simple method and evaluation of a stable $^{186/188}$Re-labeled protein. For this purpose, we selected $^{186/188}$Re(I) tricarbonyl complex as a chelating site. In this study, A7 (an IgG1 murine mAb) was used as a model protein, and $^{186/188}$Re-labeled A7 was prepared by directly reacting a $^{186/188}$Re(I) tricarbonyl precursor, $[^{186/188}Re(CO)_3(H_2O)_3]^+$, with A7. Then, in vitro stability experiments and biodistribution experiments in tumor-bearing mice were performed.

Materials and methods

Materials

^{186}Re and ^{188}W were supplied by the Japan Atomic Energy Agency (Tokai-mura, Japan) as $^{186}ReO_4^-$ and $^{188}WO_4^{2-}$ [16]. Alumina acid grade (100–200 mesh) alumina (ICN, Irvine, CA) was used as an adsorbent for the ^{188}W/^{188}Re generator. Silver cation exchange cartridges (Ag Plus) and anion exchange cartridges (SepPak QMA Light) were purchased from Alltech Associates, Inc. (Deerfield, IL) and Waters Corporation (Milford, MA), respectively. $^{188}ReO_4^-$ was eluted from a ^{188}W/^{188}Re generator using saline. The radioactive elution (5 mL) was condensed to a total of 400 μL using the method reported previously [8, 9]. A7, an immunoglobulin G1 murine mAb that recognizes the 45-kDa glycoprotein in human colon cancer, was used. A7 reacts with most colorectal cancers [17]. IsoLink kits for preparing $[^{186/188}Re(CO)_3(H_2O)_3]^+$ were obtained from Mallinckrodt (St Louis, MO). [^{125}I]Sodium iodide was purchased from PerkinElmer (Waltham, MA). Radiolabeling of A7 with ^{125}I was performed by the chloramine-T method [18]. Other reagents were of reagent grade and used as received.

The radiochemical purities of $^{186/188}$Re- and ^{125}I-labeled A7 were determined by thin layer chromatography (TLC) and cellulose acetate electrophoresis (CAE) (Separax-SP; Joko Co. Ltd., Tokyo, Japan). TLC analyses were performed with silica plates (Art 5553, Merck, Darmstadt, Germany) with a mixture of 99% methanol and 1% concentrated HCl as a developing solvent. CAE was run at an electrostatic field of 1.0 mA/cm for 20 min in veronal buffer (I = 0.06, pH 8.6).

Preparation of $^{186/188}$Re-labeled A7 ($^{186/188}$Re-$(CO)_3$-A7)

An intermediate of $^{186/188}$Re-labeled mAb, $[^{186/188}Re(CO)_3(H_2O)_3]^+$, was prepared using an IsoLink kit according to the method reported previously [19, 20]. Namely, a mixture of 400 μL $^{186/188}ReO_4^-$ and 6 μL concentrated phosphoric acid was added to an IsoLink kit to which 6 mg $BH_3{\cdot}NH_3$ (Aldrich, Milwaukee, WI) had previously been added. The reaction mixture was heated at 65°C for 15 min with a 20 mL syringe inserted to balance the pressure caused by gas production during the reaction. After the $^{186/188}$Re tricarbonyl intermediate solution was adjusted to about pH 7, 200 μL of this solution was added to 80 μL of the A7 mAb

solution (14.7 mg/mL). After 2 h of incubation at 43°C, this reaction mixture was purified with a PD-10 column (GE Healthcare UK Ltd., Buckinghamshire, England) with saline as the eluate.

In vitro stability

To evaluate its stability, ^{188}Re-$(CO)_3$-A7 in saline solution was incubated at 37°C. After incubation for 24 h, a sample was drawn and its radioactivity was analyzed by CAE and TLC. In addition, ^{188}Re-$(CO)_3$-A7 solutions were diluted 10-fold with a 0.1 M solution of histidine or freshly prepared murine plasma, and the solutions were incubated at 37°C. After 1-, 3-, and 24-h incubation, the radioactivity of each sample was analyzed by TLC.

Biodistribution in tumor-bearing mice

Experiments with animals were conducted in accordance with the Guidelines for the Care and Use of Laboratory Animals of Kanazawa University. The animals were housed with free access to food and water at 23°C with a 12-h alternating light/dark schedule. LS180 human colon carcinoma cells were obtained from ATCC (Manassas, VA) and grown in cell culture dishes in Eagle's minimum essential medium with phenol red, 10% heat-inactivated fetal calf serum, 100 μg/mL glutamine, 100 units/mL penicillin, and 100 μg/mL streptomycin. The cells were cultured in a humidified atmosphere of 95% air and 5% carbon dioxide at 37°C. They were then released from the dishes by treatment with 0.05% trypsin/EDTA. Next, to produce tumors, the mice to be inoculated were anesthetized with pentobarbital and approximately 5×10^6 cells were injected subcutaneously into the right shoulder of 4-week-old BALB/c nu/nu female mice (15–19 g). Biodistribution experiments were performed approximately 8 days postinoculation, i.e., the time required for the tumors to reach a palpable size. Groups of four or five mice were administered 100 μL ^{186}Re-$(CO)_3$-A7, ^{188}Re-$(CO)_3$-A7, or ^{125}I-A7 (7.4 kBq, A7: 100 μg, respectively) intravenously and killed at 1- and 24-h postinjection. Tissues of interest were removed and weighed, and radioactivity counts were determined with an Auto Well Gamma System (ARC-380; Aloka, Tokyo, Japan) and corrected for background radiation and physical decay during counting.

Results

Preparation of $^{186/188}$Re-$(CO)_3$-A7

In TLC analyses, $^{186/188}$Re-$(CO)_3$-A7 remained at the original position (Rf = 0), while an intermediate, $[^{186/188}Re(CO)_3(H_2O)_3]^+$, and the free perrhenate ($^{186/188}ReO_4^-$) migrated to Rf = 0.2–0.4 and Rf = 0.7–0.8, respectively [20]. In CAE analyses, intact A7 migrated to the 2–2.5 cm anode from the origin, which was determined by Ponceau S dye, and $^{186/188}$Re-$(CO)_3$-A7 also migrated to the 2–2.5 cm anode (Fig. 1), while colloidal $^{186/188}$Re remained at the origin. The radiolabeling yield of $[^{188}Re(CO)_3(H_2O)_3]^+$ was 41%. ^{186}Re-$(CO)_3$-A7 and ^{188}Re-$(CO)_3$-A7 were prepared with radiochemical yields of 23 and 28%, respectively. After purification using a PD-10 column, ^{186}Re-$(CO)_3$-A7 and ^{188}Re-$(CO)_3$-A7 showed a radiochemical purity of over 95%.

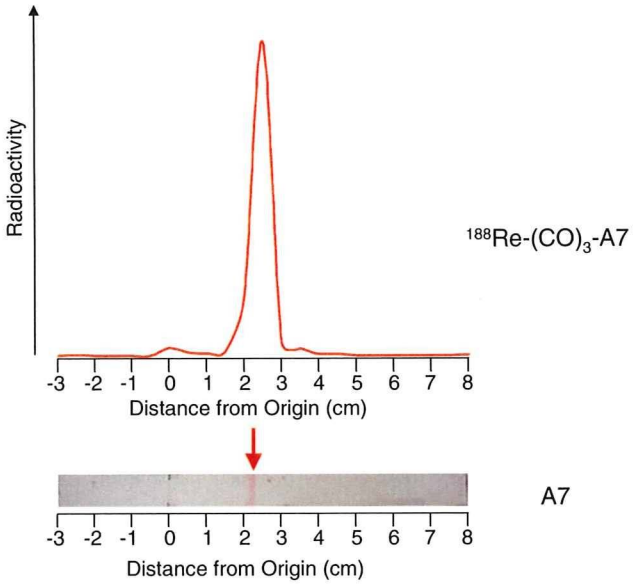

Fig. 1 Profiles of ^{188}Re-$(CO)_3$-A7 and intact A7 (Ponceau S dye) on cellulose acetate electrophoresis

In vitro stability

After incubation in saline for 24 h, about 93% of the ^{188}Re-$(CO)_3$-A7 remained intact. In murine plasma, over 90% of radioactivity existed in a protein fraction for 24 h, indicating that the ^{188}Re-$(CO)_3$-A7 is not degraded to $^{188}ReO_4^-$ in plasma. When challenged with an excess of histidine, part of the radioactivity dissociated from ^{188}Re-$(CO)_3$-A7 (Fig. 2).

Biodistribution in tumor-bearing mice

The biodistributions of ^{186}Re-$(CO)_3$-A7, ^{188}Re-$(CO)_3$-A7, and ^{125}I-A7 in tumor-bearing mice are listed in Tables 1, 2, and 3. As we expected, both radiorhenium-labeled A7 had almost identical biodistribution. ^{186}Re-$(CO)_3$-A7 and ^{188}Re-$(CO)_3$-A7 showed high uptakes in the tumors, amounting to 13.1 and 13.2% at 24-h postinjection, respectively. Meanwhile, uptake of ^{125}I-A7 in the tumor

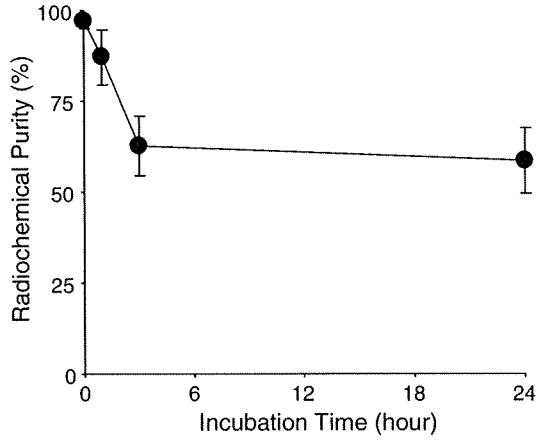

Fig. 2 Stability of ^{188}Re-$(CO)_3$-A7 in L-histidine solution

Table 1 Biodistribution of radioactivity after intravenous administration of ^{186}Re-$(CO)_3$-A7 in mice

Tissue	Time after administration	
	1 h	24 h
Blood	24.8 (1.1)	6.2 (0.3)
Tumor	5.1 (0.7)	13.1 (1.8)
Liver	18.5 (0.4)	9.7 (0.8)
Kidney	13.8 (0.4)	9.0 (1.1)
Intestine	1.5 (0.3)	2.0 (0.2)
Spleen	7.8 (1.0)	4.5 (0.9)
Pancreas	1.1 (0.1)	0.9 (0.0)
Lung	11.8 (2.5)	3.8 (0.5)
Heart	4.4 (0.6)	1.8 (0.1)
Stomach[a]	0.4 (0.0)	0.2 (0.0)
Muscle	0.9 (0.4)	0.8 (0.1)

Data are expressed as % injected dose per gram tissue. Each value represents the mean (SD) of four or five animals

[a] Data are expressed as % injected dose

was almost the same as that of $^{186/188}$Re-$(CO)_3$-A7 at 24-h postinjection. Blood clearances of $^{186/188}$Re-$(CO)_3$-A7 were faster than that of ^{125}I-A7. $^{186/188}$Re-$(CO)_3$-A7 showed that the tumor/blood ratios were over 2.0 at 24-h postinjection, but the tumor/blood ratio of ^{125}I-A7 was approximately 1.0.

Discussion

We hypothesize that the $^{186/188}Re(CO)_3$ core binds endogenous histidine residue in an antibody when $[^{186/188}Re(CO)_3(H_2O)_3]^+$ is used to label the antibody. In our preliminary experiments, we labeled H-His-OMe with $[^{186}Re(CO)_3(H_2O)_3]^+$ at room temperature, 45°C, or 100°C. As a result, the radiochemical yield increased in a

Table 2 Biodistribution of radioactivity after intravenous administration of ^{188}Re-$(CO)_3$-A7 in mice

Tissue	Time after administration	
	1 h	24 h
Blood	27.6 (1.8)	5.9 (0.8)
Tumor	6.0 (1.7)	13.2 (1.7)
Liver	18.9 (2.8)	9.7 (0.8)
Kidney	14.8 (1.7)	8.9 (0.4)
Intestine	1.8 (0.2)	2.0 (0.3)
Spleen	8.3 (0.8)	4.0 (0.7)
Pancreas	1.5 (0.2)	0.8 (0.0)
Lung	12.6 (2.2)	3.2 (0.4)
Heart	5.6 (0.5)	1.6 (0.3)
Stomach[a]	0.9 (0.2)	0.3 (0.1)
Muscle	0.8 (0.2)	0.5 (0.1)

Data are expressed as % injected dose per gram tissue. Each value represents the mean (SD) of four or five animals

[a] Data are expressed as % injected dose

Table 3 Biodistribution of radioactivity after intravenous administration of ^{125}I-A7 in mice

Tissue	Time after administration	
	1 h	24 h
Blood	36.7 (4.3)	13.6 (2.1)
Tumor	3.5 (0.7)	13.9 (3.5)
Liver	10.7 (4.5)	3.4 (1.0)
Kidney	8.3 (1.4)	2.9 (0.7)
Intestine	1.6 (0.3)	1.0 (0.3)
Spleen	7.5 (3.2)	2.5 (0.8)
Pancreas	1.3 (0.4)	1.2 (0.2)
Lung	19.8 (2.5)	7.8 (1.2)
Heart	6.9 (1.0)	3.1 (0.5)
Stomach[a]	1.2 (0.2)	1.0 (0.4)
Muscle	0.9 (0.2)	0.8 (0.1)

Data are expressed as % injected dose per gram tissue. Each value represents the mean (SD) of four animals

[a] Data are expressed as % injected dose

reaction temperature-dependent manner. In this study, A7 was reacted with $[^{186/188}Re(CO)_3(H_2O)_3]^+$ at 43°C because higher temperatures damage the antibody. Radiochemical yields of $^{186/188}$Re-labeled A7 were less than 30%. For clinical use, the radiochemical purity should be over 95% without purification. We suppose that some sequences, such as an oligohistidine sequence, could be inserted into the antibody to improve the radiochemical yield. Tait et al. [21] reported that $(His)_6$-inserted annexin V had a better radiochemical yield compared with those of $(His)_3$-inserted annexin V and wild-type annexin V when annexin V was

labeled with $[^{99m}Tc(CO)_3(H_2O)_3]^+$. Another cause of low radiochemical yields of $^{186/188}$Re-labeled A7 could be low yields of $[^{186/188}Re(CO)_3(H_2O)_3]^+$. In this study, the radiochemical yield of $[^{188}Re(CO)_3(H_2O)_3]^+$ was only 41%. Recently, higher yields of the preparation of the precursor, $[^{188}Re(CO)_3(H_2O)_3]^+$, were reported [22, 23]. We assume that using the new method for preparing $[^{186/188}Re(CO)_3(H_2O)_3]^+$ in future studies would also improve the radiochemical yields of $^{186/188}$Re-labeled A7.

The high stability of ^{188}Re-$(CO)_3$-A7 in saline and almost no degradation to $^{188}ReO_4^-$ in plasma were shown in in vitro experiments. Since accumulation in the stomach is an index of ReO_4^- in biodistribution studies [24], low radioactivity levels in the stomach after injection of $^{186/188}$Re-$(CO)_3$-A7 indicate little decomposition to $^{186/188}ReO_4^-$ in vivo. In a recent study, Chen et al. [23] prepared a ^{188}Re-labeled antibody (^{188}Re(I)-trastuzumab) by a similar method. ^{188}Re(I)-trastuzumab showed high stability in vitro and low stomach accumulation in tumor-bearing mice. These studies strongly support the validity of our results.

In other previous studies, it was reported that a radioiodine-labeled antibody, ^{88}Y-isothiocyanatobenzyl-DTPA-antibody, and ^{186}Re-MAG3-antibody showed similar blood clearances [25, 26]. However, in this study, the radioactivity (%dose/g) in blood at 24-h postinjection of ^{186}Re-$(CO)_3$-A7, ^{188}Re-$(CO)_3$-A7, and ^{125}I-A7 was 6.2 ± 0.3, 5.9 ± 0.8, and 13.9 ± 3.5, respectively. That is, $^{186/188}$Re-$(CO)_3$-A7 showed faster blood clearance compared with that of ^{125}I-A7 in the biodistribution experiments. These results suggest that $^{186/188}$Re detached from A7 in the blood flow. There is a possibility that the binding of the $^{186/188}$Re-$(CO)_3$ core to A7 is not strong, and so some molecules in the blood might remove the $^{186/188}$Re-$(CO)_3$ core from $^{186/188}$Re-$(CO)_3$-A7. Actually, when ^{188}Re-$(CO)_3$-A7 was challenged with an excess of histidine, part of the radioactivity dissociated from ^{188}Re-$(CO)_3$-A7. In this experiment, the radiochemical purity of ^{188}Re-$(CO)_3$-A7 decreased to around 60% after 3-h incubation. However, after 24-h incubation, the radiochemical purity of ^{188}Re-$(CO)_3$-A7 was almost same as that after 3-h incubation. These results suggest that there are strong and weak bindings of the ^{188}Re-$(CO)_3$ core to an A7 antibody in purified ^{188}Re-$(CO)_3$-A7 because the ^{188}Re-$(CO)_3$ core does not bind to a specific site in an antibody. Recently, the biodistribution of $[^{188}Re(CO)_3(H_2O)_3]^+$ was reported [27]. The radioactivity in blood, liver, and kidney at 24-h postinjection of $[^{188}Re(CO)_3(H_2O)_3]^+$ were 3.13 ± 0.52, 9.65 ± 1.40, and 9.62 ± 0.09, respectively. Taking into account the biodistribution at 24-h postinjection of $^{186/188}$Re-$(CO)_3$-A7 in this study, these results are also not inconsistent with our hypothesis.

Faster blood clearance is advantageous for mitigating side effects because myelosuppression is the chief side effect associated with radioimmunotherapy [28]. However, faster blood clearance compromises the accumulation of radioactivity in tumors. In summary, although diagnostic radiopharmaceuticals should be better because they need a high tumor/blood ratio at an earlier time postinjection, therapeutic radiopharmaceuticals might be unfavorable because high accumulation and long retention in tumors are preferred for a better therapeutic effect. As mentioned above, we suppose that insertion of an oligohistidine sequence could improve the radiochemical yield. In addition, insertion could also be effective from the point of view of improving the in vivo stability and biodistribution of $^{186/188}$Re-labeled antibodies.

Conclusion

$^{186/188}$Re-labeled A7 showed high uptakes in tumors the same as that of ^{125}I-labeled A7. However, further modifications of the labeling method would be necessary in order to improve radiochemical yields and their biodistribution.

References

1. Macklis RM. Radioimmunotherapy as a therapeutic option for non-Hodgkin's lymphoma. Semin Radiat Oncol. 2007;17:176–83.
2. Dillman RO. Radioimmunotherapy of B-cell lymphoma with radiolabelled anti-CD20 monoclonal antibodies. Clin Exp Med. 2006;6:1–12.
3. Davies AJ. Radioimmunotherapy for B-cell lymphoma: Y^{90} ibritumomab tiuxetan and I^{131} tositumomab. Oncogene. 2007;26:3614–28.
4. Jacene HA, Filice R, Kasecamp W, Wahl RL. Comparison of ^{90}Y-ibritumomab tiuxetan and ^{131}I-tositumomab in clinical practice. J Nucl Med. 2007;48:1767–76.
5. Garmestani K, Milenic DE, Plascjak PS, Brechbiel MW. A new and convenient method for purification of ^{86}Y using a Sr(II) selective resin and comparison of biodistribution of ^{86}Y and ^{111}In labeled Herceptin. Nucl Med Biol. 2002;29:599–606.
6. Ogawa K, Mukai T, Asano D, Kawashima H, Kinuya S, Shiba K, et al. Therapeutic effects of a ^{186}Re-complex-conjugated bisphosphonate for the palliation of metastatic bone pain in an animal model. J Nucl Med. 2007;48:122–7.
7. Ferro-Flores G, Arteaga de Murphy C. Pharmacokinetics and dosimetry of ^{188}Re-pharmaceuticals. Adv Drug Deliv Rev. 2008;60:1389–401.
8. Knapp FF Jr, Beets AL, Guhlke S, Zamora PO, Bender H, Palmedo H, et al. Availability of rhenium-188 from the alumina-based tungsten-188/rhenium-188 generator for preparation of rhenium-188-labeled radiopharmaceuticals for cancer treatment. Anticancer Res. 1997;17:1783–95.
9. Guhlke S, Beets AL, Oetjen K, Mirzadeh S, Biersack HJ, Knapp FF Jr. Simple new method for effective concentration of ^{188}Re solutions from alumina-based ^{188}W–^{188}Re generator. J Nucl Med. 2000;41:1271–8.
10. Griffiths GL, Goldenberg DM, Knapp FF Jr, Callahan AP, Chang CH, Hansen HJ. Direct radiolabeling of monoclonal antibodies

with generator-produced rhenium-188 for radioimmunotherapy: labeling and animal biodistribution studies. Cancer Res. 1991;51:4594–602.
11. Ogawa K, Mukai T, Arano Y, Ono M, Hanaoka H, Ishino S, et al. Development of a rhenium-186-labeled MAG3-conjugated bisphosphonate for the palliation of metastatic bone pain based on the concept of bifunctional radiopharmaceuticals. Bioconjug Chem. 2005;16:751–7.
12. Kinuya S, Yokoyama K, Tega H, Hiramatsu T, Konishi S, Yamamoto W, et al. Rhenium-186-mercaptoacetyltriglycine-labeled monoclonal antibody for radioimmunotherapy: in vitro assessment, in vivo kinetics and dosimetry in tumor-bearing nude mice. Jpn J Cancer Res. 1998;89:870–8.
13. Kinuya S, Yokoyama K, Kobayashi K, Motoishi S, Onoma K, Watanabe N, et al. Experimental radioimmunotherapy with ^{186}Re–MAG3–A7 anti-colorectal cancer monoclonal antibody: comparison with ^{131}I-counterpart. Ann Nucl Med. 2001;15:199–202.
14. Visser GW, Gerretsen M, Herscheid JD, Snow GB, van Dongen G. Labeling of monoclonal antibodies with rhenium-186 using the MAG3 chelate for radioimmunotherapy of cancer: a technical protocol. J Nucl Med. 1993;34:1953–63.
15. Ogawa K, Mukai T, Arano Y, Otaka A, Ueda M, Uehara T, et al. Rhenium-186-monoaminemonoamidedithiol-conjugated bisphosphonate derivatives for bone pain palliation. Nucl Med Biol. 2006;33:513–20.
16. Kobayashi K, Motoishi S, Terunuma K, Rauf AA, Hashimoto K. Production of ^{186,188}Re and recovery of tungsten from spent ^{188}W/^{188}Re generator. Radiochemistry. 2000;42:551–4.
17. Kotanagi H, Takahashi T, Masuko T, Hashimoto Y, Koyama K. A monoclonal antibody against human colon cancers. Tohoku J Exp Med. 1986;148:353–60.
18. Wilbur DS, Hadley SW, Grant LM, Hylarides MD. Radioiodinated iodobenzoyl conjugates of a monoclonal antibody Fab fragment. In vivo comparisons with chloramine-T-labeled Fab. Bioconjug Chem. 1991;2:111–6.
19. He J, Liu C, Vanderheyden JL, Liu G, Dou S, Rusckowski M, et al. Radiolabelling morpholinos with ^{188}Re tricarbonyl provides improved in vitro and in vivo stability to re-oxidation. Nucl Med Commun. 2004;25:731–6.
20. Schibli R, Schwarzbach R, Alberto R, Ortner K, Schmalle H, Dumas C, et al. Steps toward high specific activity labeling of biomolecules for therapeutic application: preparation of precursor $[^{188}Re(H_2O)_3(CO)_3]^+$ and synthesis of tailor-made bifunctional ligand systems. Bioconjug Chem. 2002;13:750–6.
21. Tait JF, Smith C, Gibson DF. Development of annexin V mutants suitable for labeling with Tc(i)-carbonyl complex. Bioconjug Chem. 2002;13:1119–23.
22. Park SH, Seifert S, Pietzsch HJ. Novel and efficient preparation of precursor $[^{188}Re(OH_2)_3(CO)_3]^+$ for the labeling of biomolecules. Bioconjug Chem. 2006;17:223–5.
23. Chen KT, Lee TW, Lo JM. In vivo examination of ^{188}Re(I)-tricarbonyl-labeled trastuzumab to target HER2-overexpressing breast cancer. Nucl Med Biol. 2009;36:355–61.
24. Lin WY, Hsieh JF, Tsai SC, Yen TC, Wang SJ, Knapp FF Jr. A comprehensive study on the blockage of thyroid and gastric uptakes of ^{188}Re-perrhenate in endovascular irradiation using liquid-filled balloon to prevent restenosis. Nucl Med Biol. 2000;27:83–7.
25. Brouwers AH, van Eerd JE, Frielink C, Oosterwijk E, Oyen WJ, Corstens FH, et al. Optimization of radioimmunotherapy of renal cell carcinoma: labeling of monoclonal antibody cG250 with ^{131}I, ^{90}Y, ^{177}Lu, or ^{186}Re. J Nucl Med. 2004;45:327–37.
26. Koppe MJ, Bleichrodt RP, Soede AC, Verhofstad AA, Goldenberg DM, Oyen WJ, et al. Biodistribution and therapeutic efficacy of $^{125/131}$I-, ^{186}Re-, $^{88/90}$Y-, or ^{177}Lu-labeled monoclonal antibody MN-14 to carcinoembryonic antigen in mice with small peritoneal metastases of colorectal origin. J Nucl Med. 2004;45:1224–32.
27. Xia JY, Wang YX, Li GC, Yu JF, Yin DZ. Synthesis of pyridyl derivatives for the future functionalization of biomolecules labeled with the fac-$[Re\text{-}188(CO)_3(H_2O)_3]^+$ precursor. J Radioanal Nucl Chem. 2009;279:245–52.
28. Oriuchi N, Higuchi T, Hanaoka H, Iida Y, Endo K. Current status of cancer therapy with radiolabeled monoclonal antibody. Ann Nucl Med. 2005;19:355–65.

Eur J Nucl Med Mol Imaging
DOI 10.1007/s00259-010-1467-4

ORIGINAL ARTICLE

Rapid detection of hypoxia-inducible factor-1-active tumours: pretargeted imaging with a protein degrading in a mechanism similar to hypoxia-inducible factor-1α

Masashi Ueda · Takashi Kudo · Yuji Kuge · Takahiro Mukai · Shotaro Tanaka · Hiroaki Konishi · Azusa Miyano · Masahiro Ono · Shinae Kizaka-Kondoh · Masahiro Hiraoka · Hideo Saji

Received: 8 December 2009 / Accepted: 29 March 2010

Abstract
Purpose Hypoxia-inducible factor-1 (HIF-1) plays an important role in malignant tumour progression. For the imaging of HIF-1-active tumours, we previously developed a protein, POS, which is effectively delivered to and selectively stabilized in HIF-1-active cells, and a radioiodinated biotin derivative, (3-^{123}I-iodobenzoyl)norbiotinamide (^{123}I-IBB), which can bind to the streptavidin moiety of POS. In this study, we aimed to investigate the feasibility of the pretargeting method using POS and ^{123}I-IBB for rapid imaging of HIF-1-active tumours.
Methods Tumour-implanted mice were pretargeted with POS. After 24 h, ^{125}I-IBB was administered and subsequently, the biodistribution of radioactivity was investigated at several time points. In vivo planar imaging, comparison between ^{125}I-IBB accumulation and HIF-1 transcriptional activity, and autoradiography were performed at 6 h after the administration of ^{125}I-IBB. The same sections that were used in autoradiographic analysis were subjected to HIF-1α immunohistochemistry.
Results ^{125}I-IBB accumulation was observed in tumours of mice pretargeted with POS (1.6%ID/g at 6 h). This result is comparable to the data derived from ^{125}I-IBB-conjugated POS-treated mice (1.4%ID/g at 24 h). In vivo planar imaging provided clear tumour images. The tumoral accumulation of ^{125}I-IBB significantly correlated with HIF-1-dependent luciferase bioluminescence (R=0.84, p<0.01). The intratumoral distribution of ^{125}I-IBB was heterogeneous and was significantly correlated with HIF-1α-positive regions (R=0.58, p<0.0001).
Conclusion POS pretargeting with ^{123}I-IBB is a useful technique in the rapid imaging and detection of HIF-1-active regions in tumours.

Keywords Tumour hypoxia · Hypoxia-inducible factor-1 (HIF-1) · Oxygen-dependent degradation (ODD) · Molecular imaging · Pretargeting

M. Ueda
Radioisotopes Research Laboratory, Kyoto University Hospital,
Faculty of Medicine, Kyoto University,
54 Shogoin Kawahara-cho, Sakyo-ku,
Kyoto 606-8507, Japan

M. Ueda · T. Kudo · Y. Kuge · H. Konishi · A. Miyano · M. Ono · H. Saji (✉)
Department of Patho-Functional Bioanalysis,
Graduate School of Pharmaceutical Sciences, Kyoto University,
46-29 Yoshida Shimoadachi-cho, Sakyo-ku,
Kyoto 606-8501, Japan
e-mail: hsaji@pharm.kyoto-u.ac.jp

Y. Kuge
Central Institute of Isotope Science, Hokkaido University,
Kita 15, Nishi 7, Kita-ku,
Sapporo 060-0815, Japan

T. Mukai
Department of Biomolecular Recognition Chemistry,
Graduate School of Pharmaceutical Sciences, Kyushu University,
3-1-1 Maidashi, Higashi-ku,
Fukuoka 812-8582, Japan

S. Tanaka · S. Kizaka-Kondoh · M. Hiraoka
Department of Radiation Oncology and Image-applied Therapy,
Graduate School of Medicine, Kyoto University,
54 Shogoin Kawahara-cho, Sakyo-ku,
Kyoto 606-8507, Japan

Published online: 29 April 2010

Introduction

Insufficient blood supply to a rapidly growing tumour leads to the presence of an oxygen tension below physiological

levels, i.e. hypoxia, in solid tumours [1]. Tumour hypoxia is critically important in tumour physiology and cancer treatment, and it appears to be strongly associated with malignant progression and therapy resistance. The transcription factor, hypoxia-inducible factor-1 (HIF-1) is induced in hypoxic regions. It is a master regulator of the genes that encode for angiogenic and metastatic factors, and plays an important role in tumour progression [2–4]. Thus, noninvasive imaging of HIF-1-active regions in tumours would be useful for characterizing tumours and determining a course of therapy.

HIF-1 is a heterodimer that consists of an oxygen-sensitive alpha subunit (HIF-1α) and a constitutively expressed beta subunit. In normoxia, two proline residues in the oxygen-dependent degradation (ODD) domain of HIF-1α are hydroxylated, leading to a proteasomal degradation of HIF-1α. Under hypoxic conditions, oxygen is the rate-limiting factor for prolyl hydroxylation, resulting in a decreased degradation of HIF-1α [5, 6]. That is to say, the ODD domain of HIF-1α is responsible for the regulation of HIF-1 activity. Thus, it is likely that a probe containing the ODD domain and degrading in a manner similar to HIF-1α could be used to evaluate HIF-1 activity in vivo.

We have recently developed proteins in which the protein transduction domain (PTD) is fused to the ODD domain and demonstrated the specificity of these proteins to HIF-1-active cells [7–11]. In a previous study, we also fused the PTD-ODD with a monomeric streptavidin (SAV) to produce a chimeric protein, PTD-ODD-SAV (POS); we also synthesized a radiolabelled biotin derivative, (3-$^{123/125}$I-iodobenzoyl)norbiotinamide ($^{123/125}$I-IBB). For nuclear medical imaging, the two were conjugated to give $^{123/125}$I-IPOS, the characterization of which has been presented previously [9]. In brief, POS was degraded in an oxygen-dependent manner and a clear tumour image was obtained 24 h after injection of ^{123}I-IPOS. In addition, the tumoral accumulation correlated with HIF-1 activity and the intratumoral distribution of ^{125}I-IPOS was heterogeneous and corresponded to hypoxic areas. These findings suggested that ^{123}I-IPOS is a potential probe for the imaging of HIF-1-active tumours. However, due to its large molecular size, ^{123}I-IPOS cleared from the blood slowly; thus, we could not obtain a high tumour-to-normal tissue ratio within a short time after probe injection.

To overcome this problem, we propose a pretargeting method based on the high-affinity interaction between SAV and biotin [12]. This method uses a combination of tumour-seeking molecules and the prompt clearance of low-molecular-weight radiolabelled compounds (effector molecules) that are cleared within minutes from the blood. One of the advantages of the pretargeting method is that it provides a high tumour-to-normal tissue ratio within a short time after injection. In addition, because the effector molecules used in this method are rapidly cleared from the body, radiation exposure is reduced. Moreover, some recent studies have shown that the tumour uptake of the effector molecules used in the pretargeting method is identical to or even higher than that of directly radiolabelled antibody. The images and therapeutic effects shown in these studies were significantly improved [13–15]. In the present study, we aimed to reveal the effectiveness of the pretargeting method using POS and ^{123}I-IBB in the rapid imaging of HIF-1-active tumour hypoxia.

Materials and methods

Cells and cell culture

FM3A mouse mammary tumour cells were purchased from Health Science Research Resources Bank (Osaka, Japan) and were cultured in 10% fetal bovine serum/RPMI-1640 medium (Nissui Pharmaceutical, Tokyo, Japan). Suit2 human pancreatic tumour cells that express luciferase in response to HIF-1 activity (Suit2/Luc cells) were established by Prof. Kizaka-Kondoh [16]. These cells were authenticated by s multiplex PCR method using short tandem repeat and were maintained in 10% fetal bovine serum/Dulbecco's modified Eagle's medium (Nissui Pharmaceutical). The culture media were supplemented with penicillin (100 U/ml) and streptomycin (100 μg/ml). Cells were incubated at 37°C in a well-humidified incubator with 5% CO_2 and 95% air.

Preparation of fusion protein

POS was overexpressed in *Escherichia coli* and purified as described in a previous report [9]. Purified POS was then dissolved in Tris-HCl buffer (pH 8.0).

Synthesis

Ammonium ^{123}I-iodide was kindly provided by Nihon Medi-Physics (Hyogo, Japan). Sodium ^{125}I-iodide was purchased from PerkinElmer Life and Analytical Sciences (Boston, MA). All other chemicals used in this study were of reagent grade and are commercially available. $^{123/125}$I-IBB and nonradioactive IBB were synthesized as described in a previous report [9, 17]. ^{123}I-IPOS was obtained by incubating ^{123}I-IBB and POS for 1 h, followed by purification on Sephadex G50 columns (GE Healthcare Bioscience, Uppsala, Sweden).

Animal model

Animal studies were conducted in accordance with our institutional guidelines, and the experimental procedures

were approved by the Kyoto University Animal Care Committee. Female C3H/He mice and BALB/c *nu/nu* mice at 5 weeks of age were purchased from Japan SLC (Hamamatsu, Japan). FM3A and Suit2/Luc tumour models were prepared as described in a previous report [9]. The cells were subcutaneously implanted in the right thigh, except in the mice that were to be used for the bioluminescence imaging in which the cells were subcutaneously implanted in both thighs. After tumour implantation, mice were fed an AIN76-A-based, biotin-free diet (Oriental Yeast Company, Tokyo, Japan) in order to prevent dietary biotin from inhibiting the binding of ^{125}I-IBB to POS. The mice were subjected to a tracer study 2 weeks after implantation. The average diameter and average volume of the tumours were 8 mm and 350 mm^3, respectively.

Biodistribution

^{125}I-IBB (37 kBq) was injected intravenously into FM3A-implanted mice (n=3–5), and at 1, 3, 6 and 24 h after injection, the mice were killed. For the pretargeting study, the mice (n=5) were injected with 30 μg of POS and 24 h later ^{125}I-IBB was injected intravenously. The mice were killed at the same time points as above. Whole organs were immediately removed and weighed, and their radioactivity was measured with an autowell gamma counter (ARC2000; Aloka, Tokyo, Japan). The results are expressed in terms of the percent injected dose per gram of tissue (%ID/g).

In vivo blocking study

FM3A-implanted mice (n=5) were pretargeted with POS (30 μg); 24 h later, ^{125}I-IBB (37 kBq) was injected intravenously, with or without D-biotin (1 nmol) or with unlabelled IBB (500 pmol). Six hours after ^{125}I-IBB administration, the mice were killed. Whole organs were immediately removed and weighed, and their radioactivity was measured with the gamma counter (ARC2000). The results are expressed as %ID/g.

Size-exclusion analysis of radioactive compounds in tumours

FM3A-implanted mice (n=5) were pretargeted with POS (30 μg), and 24 h later, ^{125}I-IBB (8.0 MBq) was injected intravenously. The mice were killed 6 h after the injection of ^{125}I-IBB, and the tumours were removed. Extracts were prepared according to a previously reported method [18], with slight modification. In brief, the tumours were homogenized in ice-cold 0.1 *M* Tris-HCl buffer containing 0.15 *M* NaCl (pH 6.5), using a Polytron homogenizer (PT10-35, Kinematica, Switzerland). The preparations were then centrifuged at 4°C and 5,000×*g* for 30 min (Micro Cooling Centrifuge 5922; Kubota, Osaka, Japan). The supernatants were filtered through a 0.46-μm filter (Nacalai Tesque, Kyoto, Japan) and analysed by size-exclusion chromatography using a PD-10 column (GE Healthcare Bioscience).

In vivo imaging

A SPECT-2000H scanner (Hitachi Medical, Tokyo, Japan) equipped with a low-energy, high-resolution, parallel-hole collimator [19, 20] was used. For direct targeting (n=4), ^{123}I-IPOS (30 μg, 4.9–7.4 MBq) was injected intravenously into each FM3A-implanted mouse. For the pretargeting method (n=5), ^{123}I-IBB (3.1–16 MBq) was injected into a tail vein 24 h after pretargeting with POS (30 μg). Under 2.5% halothane anaesthesia, the mice were placed on a scanner bed in the prone position. Planar images were obtained at 24 h after the injection of ^{123}I-IPOS in mice in the direct-targeted group or at 6 h after the injection of ^{123}I-IBB in mice in the pretargeted group. The image acquisition time was 10 min for both the groups. Regions of interest (ROI) were set on the tumour in the right thigh and the corresponding area in the left thigh.

Comparison between ^{125}I-IBB accumulation and HIF-1 transcriptional activity in the same tumours in mice pretargeted with POS

The Suit2/Luc-implanted mice (n=5) were pretargeted with POS (30 μg) and 24 h later, ^{125}I-IBB (37 kBq) was injected intravenously. After 5.5 h, 200 μl of D-luciferin solution (10 mg/ml in PBS; VivoGlo Luciferin, Promega, WI) was injected intraperitoneally. After 20 min, the mice were anaesthetized with 2.5% isoflurane and imaged according to a previously described method [9]. After bioluminescence imaging, the mice were killed and the radioactivity in each tumour was measured.

Autoradiography

Autoradiographic studies were performed in Suit2/Luc-implanted mice (n=6). The mice were pretargeted with POS (30 μg) and 24 h later, ^{125}I-IBB (4.1 MBq) was injected intravenously. After another 4 h, pimonidazole (PIMO, 60 mg/kg) was injected intraperitoneally and the mice were killed 2 h later. Autoradiograms were then obtained and analysed according to a previously described method [19–21]. The adjacent section on each autoradiogram was stained with haematoxylin-eosin to identify regions of necrosis.

Immunohistochemistry

The slides used in the autoradiographic study were subjected to dual fluorescent immunostaining for HIF-1α

and PIMO. The sections were fixed in 2% paraformaldehyde and ice-cold methanol, blocked with Protein Block Serum Free (Dako, Glostrup, Denmark), and treated with anti-human/mouse HIF-1α polyclonal antibody (R&D Systems, Minneapolis, MN) as a primary antibody. The specific signals were detected using an Alexa Fluor 568-conjugated $F(ab')_2$ fragment of goat anti-rabbit antibody (Invitrogen, San Diego, CA). Thereafter, after washing with PBS, FITC-conjugated mouse IgG_1 monoclonal antibody (Chemicon, Temecula, CA) was treated according to the manufacturer's protocol for PIMO staining. The sections were then dried and coverslipped using an antifade reagent (ProLong Gold; Invitrogen). To evaluate the specificity of the HIF-1α signal, negative control rabbit immunoglobulin (Dako) was incubated with the adjacent sections, instead of the primary antibody. To evaluate the specificity of the PIMO signal, tumour sections derived from PIMO-untreated mice were stained following the same protocol. Fluorescent microscopic images were obtained by BIO-REVO BZ-9000 (Keyence, Osaka, Japan).

Image analysis

The autoradiograms were quantified using MultiGauge software (ver. 3.0, Fuji Photo Film, Tokyo, Japan) and the immunohistochemical images were analysed using BZ analyser software (Keyence). ROIs were set in identical positions in both images on the basis of the x- and y-position of each ROI displayed in both software programs. The necrotic regions were excluded from the analysis. We set 10–14 ROIs (area 1 mm^2) on the autoradiogram of each tumour and then transferred them to the corresponding immunohistochemical image. The radioactivity in each ROI was expressed in terms of percent injected dose. The expression densities of HIF-1α and PIMO were determined in terms of the percentage of the positively stained region.

Statistical analyses

The two groups were compared using the Mann-Whitney *U* test, and correlation coefficients were assessed using the Spearman rank analysis. A chi-squared test was used to compare the correlation coefficients between ^{125}I-IBB accumulation and HIF-1α expression and PIMO adduct formation. Values of $p < 0.05$ were considered statistically significant.

Results

Radiosynthesis of $^{123/125}$I-IBB and ^{123}I-IPOS

^{123}I-IBB and ^{125}I-IBB were obtained in the absence of a carrier and with radiochemical yields of 29% and 65% and radiochemical purities of greater than 95% and greater than 94%, respectively. ^{123}I-IPOS was obtained with a radiochemical yield of 90% and a radiochemical purity of greater than 99%.

Biodistribution

An examination of the biodistribution of ^{125}I-IBB alone revealed that the tumour-to-blood ratio was less than 1 at all time points. This indicated that ^{125}I-IBB did not accumulate in the tumours. The radioactivity in the stomach was low indicating the resistance of ^{125}I-IBB to deiodination in vivo (Table 1). In contrast, in the pretargeted group, the tumour-to-blood ratio was greater than 1 as early as 1 h after the injection of ^{125}I-IBB and the tumour-to-blood ratio increased in a time-dependent manner (Table 2). The blood clearance in both groups was comparable. In the pretargeted group, tumour accumulation of ^{125}I-IBB 6 h after injection was 1.58±0.42%ID/g, which was more than 30-fold higher than for ^{125}I-IBB alone (0.05±0.01%ID/g). The radioactivity in the normal tissues decreased more rapidly than in the

Table 1 Biodistribution of ^{125}I-IBB in FM3A-implanted mice

Organ	Time after injection (h)			
	1	3	6	24
Blood	1.12±0.43	0.33±0.01	0.15±0.00	0.03±0.01
Liver	6.36±1.70	1.21±0.04	0.20±0.04	0.02±0.01
Heart	1.27±0.31	0.26±0.01	0.07±0.04	0.02±0.02
Lung	1.14±0.22	0.30±0.04	0.10±0.03	0.02±0.01
Kidney	5.54±0.74	1.06±0.23	0.35±0.18	0.07±0.02
Stomach	0.62±0.13	0.35±0.23	0.33±0.24	0.12±0.10
Intestine	32.61±8.24	24.73±12.12	10.69±4.93	0.95±0.64
Tumour	0.53±0.14	0.13±0.04	0.05±0.01	0.01±0.01
Muscle	0.84±0.18	0.15±0.05	0.03±0.02	0.01±0.01
Tumour/blood ratio	0.49±0.14	0.39±0.09	0.36±0.09	0.57±0.57

Organ uptake values are means ±SD (n=3–5) in units of percent injected dose per gram of tissue, except for the stomach (percent injected dose) and tumour/blood ratio

Table 2 Biodistribution of ^{125}I-IBB in FM3A-implanted mice pretargeted with POS

Organ	Time after injection (h)			
	1	3	6	24
Blood	1.28±0.22	0.58±0.05	0.37±0.05	0.05±0.01
Liver	10.16±0.98	5.56±0.74	4.07±0.38	0.57±0.15
Heart	1.77±0.11	0.90±0.12	0.59±0.08	0.06±0.02
Lung	1.98±0.24	0.95±0.13	0.67±0.07	0.08±0.01
Kidney	25.09±1.42	11.58±2.46	5.78±1.02	0.30±0.04
Stomach	0.63±0.15	0.56±0.17	0.34±0.20	0.08±0.05
Intestine	22.45±3.40	20.11±7.22	8.66±6.13	0.76±0.42
Tumour	2.73±0.67	2.03±0.16	1.58±0.42	0.59±0.23
Muscle	1.04±0.16	0.47±0.13	0.30±0.11	0.04±0.02
Tumour/blood ratio	2.15±0.39	3.51±0.26	4.23±0.81	13.13±4.58

Organ uptake values are means ±SD (n=5) in units of percent injected dose per gram of tissue, except for the stomach (percent injected dose) and tumour/blood ratio

tumour. The radioactivity in the tumour at 24 h after injection was the second highest among the organs examined and both the tumour-to-blood and tumour-to-muscle ratios further increased (Table 2).

Tumour uptake of ^{125}I-IBB was significantly reduced to 46% following treatment with nonradioactive IBB (Table 3). Concomitant treatment with D-biotin also resulted in a 37% decrease in tumour uptake of ^{125}I-IBB (data not shown). ^{125}I-IBB accumulation in other tissues, except the blood, decreased following treatment with nonradioactive IBB.

Size-exclusion analysis of radioactive compounds in tumours

The recovery of radioactivity from tumour homogenates was 95.7±7.2%, and that from the PD-10 columns was 85.5±6.9%. A major proportion of the radioactivity was eluted in a macromolecular fraction (78.7±6.7%).

Table 3 Blocking study of the biodistribution of ^{125}I-IBB in FM3A-implanted mice pretargeted with POS

Organ	Vehicle	IBB treatment
Blood	0.36±0.18	0.48±0.10
Liver	5.26±0.61	2.58±0.69*
Heart	0.76±0.09	0.38±0.08
Lung	1.09±0.25	0.48±0.12
Kidney	12.15±5.03	2.44±0.41**
Stomach	0.82±0.48	0.25±0.04
Intestine	9.04±3.77	5.06±2.30
Tumour	1.95±0.63	0.90±0.18*
Muscle	0.51±0.06	0.16±0.04***
Tumour/blood ratio	5.49±1.12	1.93±0.38****

Organ uptake values are means±SD (n=5) in units of percent injected dose per gram of tissue, except for the stomach (percent injected dose) and tumour/blood ratio

*p<0.005, **p<0.001, ***p<0.0005, ****p<0.0001 vs. vehicle group

In vivo imaging

Figure 1a shows the accumulation of ^{123}I-IBB in the POS-pretargeted tumour. The tumour was clearly visualized 6 h after ^{123}I-IBB injection, and the calculated tumour-to-muscle ratio was 4.6±1.4. The image was comparable to that obtained 24 h after ^{123}I-IPOS injection, using the direct-targeting method (Fig. 1b; tumour-to-muscle ratio 6.9±1.6). Compared to the direct targeting method, with the pretargeting method, radioactivity decreased in the liver, but increased in the intestine. These findings were consistent with the biodistribution study data.

^{125}I-IBB accumulation vs. HIF-1 transcriptional activity in tumours in mice pretargeted with POS

Figure 2 shows a positive correlation between HIF-1-induced luciferase bioluminescence and ^{125}I-IBB accumulation 6 h after injection in tumours in mice pretargeted with POS (R=0.84, p<0.01).

Regional distribution of ^{125}I-IBB in the POS-pretargeted tumour

Dual fluorescent immunohistochemistry revealed the presence of HIF-1α- and PIMO-positive hypoxic areas in the tumour (Fig. 3a, b). The sections derived from PIMO-untreated mice were not stained with anti-PIMO antibody, and the HIF-1α signal was not detected in the negative control antibody-treated sections (data not shown). The autoradiogram showed that the distribution of ^{125}I-IBB in the tumour was heterogeneous (Fig. 3c) and, for the most part, corresponded to the HIF-1α- and PIMO-positive hypoxic areas. However, there were also a few regions where the signal for HIF-1α or PIMO was positive, but where ^{125}I-IBB had not accumulated (Fig. 3d, e). High-magnification merged imaging of HIF-1α and PIMO immunostaining revealed that HIF-1α-positive regions and

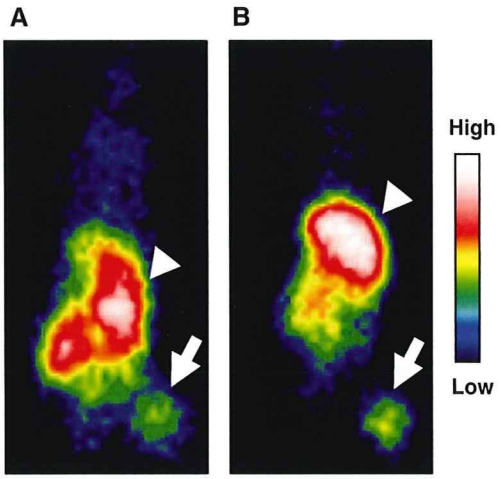

Fig. 1 Typical planar images of FM3A-implanted mice acquired in the pretargeting method (**a**) and the direct-targeting method (**b**). Images were acquired 6 h after injection of ^{123}I-IBB in the pretargeting method and 24 h after injection of ^{123}I-IPOS in the direct targeting method. Tumours are clearly visualized (*arrows*) in a similar fashion in both images (*arrowheads* **a** intestine, **b** liver)

PIMO-positive regions were not always identical; some regions were positive for both, while other regions did not match (Fig. 3f). Therefore, we compared correlations between ^{125}I-IBB accumulation and the expression of HIF-1α and PIMO. As shown in Fig. 4, significant positive correlations were found between the regional accumulation of ^{125}I-IBB in POS-pretargeted tumour sections and the expression of both hypoxic markers (HIF-1α R=0.58, p<0.0001; PIMO R=0.34, p<0.005). The correlation coefficient between ^{125}I-IBB and HIF-1α was greater than that with PIMO, although the difference was not statistically significant (χ^2=3.13, p=0.077).

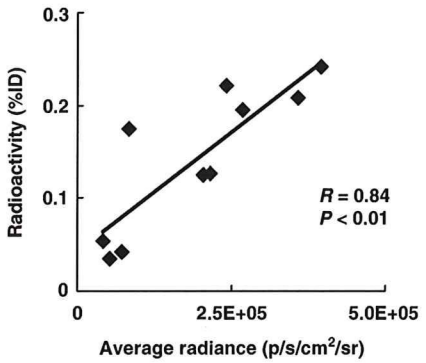

Fig. 2 Correlation between ^{125}I-IBB accumulation and HIF-1 transcriptional activity in the same tumour in mice pretargeted with POS. Mice carrying tumours with the HIF-1-dependent luciferase reporter gene in both thighs were used. The ordinate represents accumulated radioactivity (%ID), and the abscissa represents HIF-1-dependent luciferase bioluminescence. The correlation coefficient (R) was 0.84, indicating a highly significant correlation (p<0.01)

Discussion

In the study reported here we showed rapid tumour imaging following pretargeting using POS and $^{123/125}$I-IBB. Using the pretargeting method, the tumoral accumulation (1.6% ID/g) and the tumour-to-blood ratio (4.2) 6 h after injection were found to be comparable to the data obtained 24 h after ^{125}I-IPOS injection (1.4%ID/g, 5.1) [9]. The scintigraphic images of mice targeted with ^{123}I-IPOS were very similar to those of prior studies, in which high signal levels were detected in the tumour, although the highest activity was seen in the liver even 24 h after injection [9]. In contrast, the images of the pretargeted mice clearly showed that ^{123}I-IBB accumulated in the tumour more rapidly and cleared much more promptly from the body (with the exception of the intestine) than ^{123}I-IPOS. These results indicate that the pretargeting method allows a shortening of the waiting time to one-fourth that required for direct targeting to obtain an adequate image. Clinical application of the pretargeting method in the future will contribute to a reduction in radiation exposure of the patient.

Recently it has been suggested that HIF-1 activates a number of genes, such as VEGF, erythropoietin, matrix metalloproteinase and glucose transporter, and that the expression level of HIF-1 correlates with a poor prognosis in many tumours [22–26]. Furthermore, the activation of such genes has an important role with respect to aggressive cancer phenotypes. Therefore, visualization and tumour therapy targeting for HIF-1 activation may be an important supplement to imaging of hypoxia per se when characterizing tumours. Some hypoxia imaging probes, including ^{18}F-fluoromisonidazole (^{18}F-FMISO), 1-α-D-(5-deoxy-5-^{18}F-fluoroarabinofuranosyl)-2-nitroimidazole (^{18}F-FAZA) and ^{64}Cu-diacetyl-bis(N^4-methylthiosemicarbazone) (^{64}Cu-ATSM), have been developed [27]. They detect physically low oxygen pressure (<10 mmHg) and are useful in predicting the efficacy of radiotherapy [28]. However, the mechanisms underlying hypoxic accumulation of such probes are not dependent on HIF-1 expression [29]. Previously reported HIF-1-activity imaging systems required exogenous reporter gene transcription, which presents difficulties in practice [30, 31]. In contrast, our approach could assess HIF-1-activity directly, via a two-step targeting of the probes.

A recent immunohistochemical study has demonstrated the lack of complete colocalization between HIF-1α and PIMO. Sobhanifar et al. have reported that HIF-1 is expressed at higher levels of oxygen than those that allow PIMO metabolism and binding [32]. Thus, we compared the correlation between ^{125}I-IBB accumulation and HIF-1α- and PIMO-positive regions. As shown in Fig. 4, the correlation coefficient between ^{125}I-IBB and HIF-1α was greater than that between ^{125}I-IBB and PIMO, although the

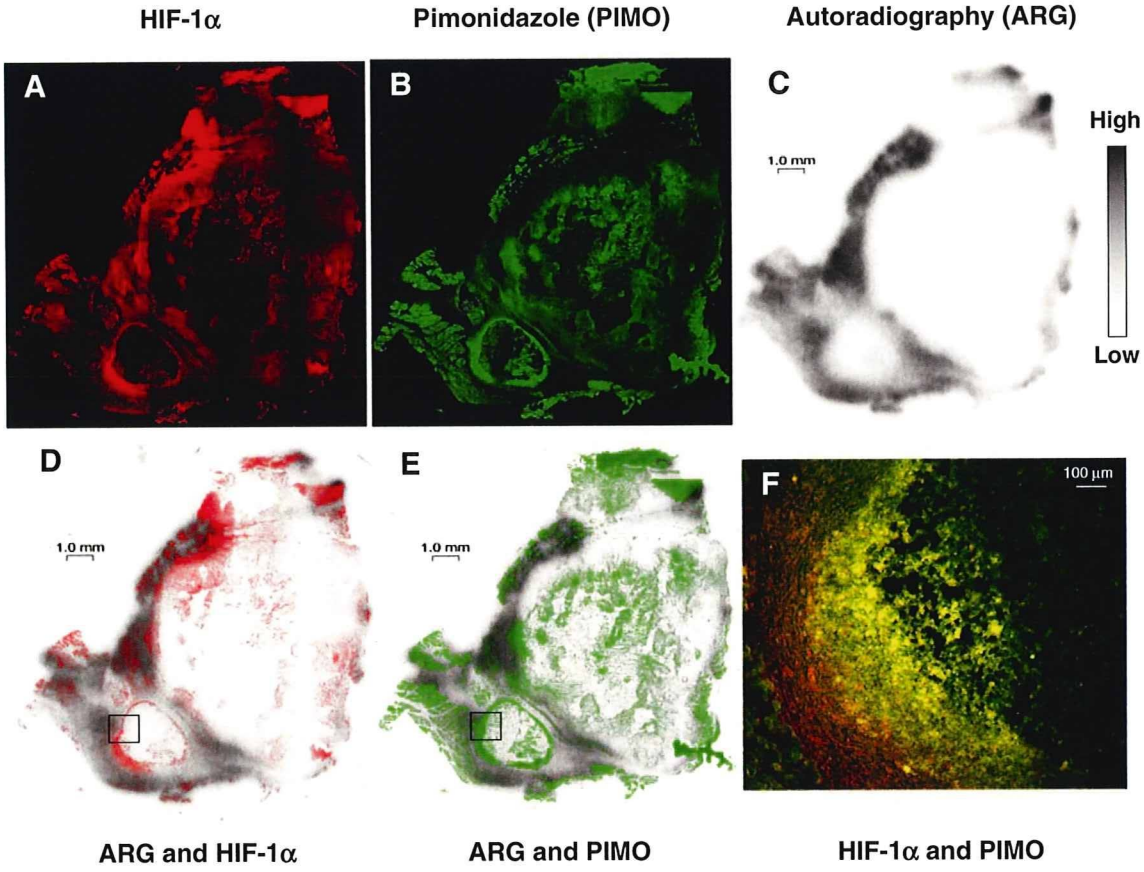

Fig. 3 Comparison between the intratumoral distribution of ^{125}I-IBB and the HIF-1α- and PIMO-positive hypoxic regions in POS-pretargeted tumours. **a–c** Typical images of HIF-1α immunostaining (**a**), PIMO immunostaining (**b**) and from autoradiography (**c**) in the same section. **d**, **e** Autoradiography image merged with HIF-1α immunostaining (**d**) and PIMO immunostaining (**e**) images. **f** High-magnification merged image of HIF-1α immunostaining and PIMO immunostaining (from insets in **d** and **e**). Some regions are both positive (*yellow*) and others do not match (*red* and *green*)

difference between the two correlation coefficients was not statistically significant. Therefore, the regions showing ^{125}I-IBB accumulation potentially corresponded to the HIF-1α-positive regions and to the PIMO-positive regions but to a lesser degree. However, in the present study, the HIF-1α-positive region was mainly detected both in the PIMO-positive regions and in the surrounding regions (Fig. 3f). This result is consistent with those of a previous study, which showed that carbonic anhydrase 9, a HIF-1-regulated protein, generally colocates with PIMO though displaying greater extension in the direction of perfused areas [33]. Due to the overlap, the region showing ^{125}I-IBB accumu-

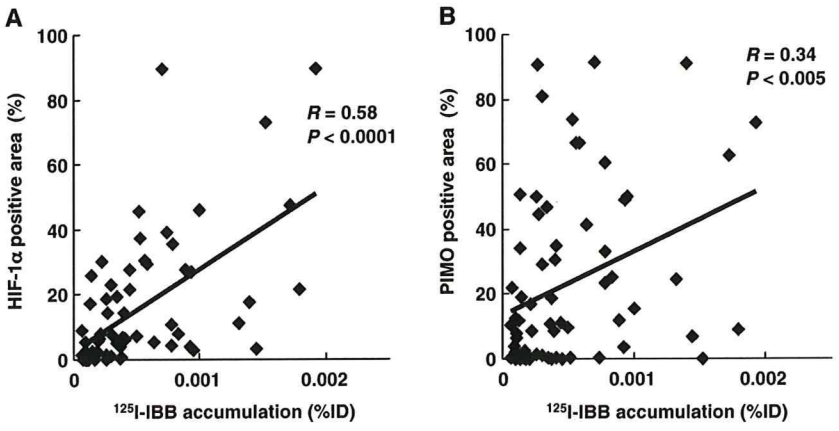

Fig. 4 Correlation between areas showing ^{125}I-IBB accumulation and HIF-1α- and PIMO-positive areas in POS-pretargeted tumours. A total of six sections (one section per tumour) were analysed. Quantitative analysis of autoradiograms provided data on ^{125}I-IBB accumulation. ^{125}I-IBB accumulation was positively correlated with HIF-1α and PIMO expression (HIF-1α R=0.58, p<0.0001; PIMO R=0.34, p<0.005)

lation also showed a weak positive correlation with the PIMO-positive regions. On the other hand, there were a few HIF-1α-negative regions in which ^{125}I-IBB accumulated (Fig. 3d). This discrepancy could be explained by the delivery of POS and/or ^{125}I-IBB. Since both probes were delivered by blood flow, they potentially tended to accumulate in regions rich in blood vessels, i.e. HIF-1α-negative regions. Because the degradation rate of POS was relatively slow [9], an excess of POS delivered to HIF-1α-negative regions could not be degraded, resulting in ^{125}I-IBB accumulation in these regions. POS contains not only the essential domain related to the oxygen-dependent degradation of HIF-1α, but also PTD and SAV. These modifications may lower the rate of degradation, and this is a drawback of POS. However, it should be noted that by using the pretargeting method with POS and ^{123}I-IBB, radioactivity accumulation was significantly correlated with the HIF-1α-positive region (Fig. 4a). Furthermore, accumulation of ^{123}I-IBB was correlated with HIF-1 transcriptional activity in the tumours in mice pretargeted with POS (Fig. 2). Thus, our approach would detect not only hypoxic regions, but also HIF-1-active regions, and thus this approach could prove important to the qualitative diagnosis of and effective therapy against cancer.

In the pretargeting study, ^{125}I-IBB accumulated in the tumours of POS-pretargeted mice. The accumulation was inhibited by nonradioactive IBB and D-biotin. Moreover, most of the radioactivity in the tumour existed as macromolecules. Taken together, the radioactivity in the tumour was caused by the binding of ^{125}I-IBB to the SAV moiety of POS. Thus, ^{125}I-IBB has the ability to bind to SAV, not only in vitro but also in vivo. It has been reported that the expression of HIF-1 is not ubiquitous, but heterogeneous, and is small in tumours [34]. Accumulation of the probe in tumours harbouring HIF-1-dependent reporter genes has been reported to be approximately 1%ID/g [34–36], which is comparable to the results of the present study.

In the biodistribution study of ^{125}I-IBB alone, accumulation of radioactivity was highest in the intestine. This tissue distribution pattern reflects the behaviour of radioiodinated biotin itself, since ^{125}I-IBB is not cleaved by serum biotinidase [17]. The high accumulation of ^{125}I-IBB in the intestine resulted in high background activity in the abdominal region; therefore, the imaging of abdominal HIF-1-active tumours would be difficult. In this case, biotin derivatives that show faster clearance from the abdominal region than ^{125}I-IBB are required. However, the background radioactivity in the thoracic region and cervicofacial region was generally low. The expression of HIF-1 has been reported to be associated with a poor prognosis in breast and lung cancers and in head and neck squamous cell carcinomas [26, 37, 38]; therefore, our imaging approach would be particularly useful for detecting HIF-1 activity in these tumours.

Recent studies have revealed that HIF-1 levels are controlled not only at the post-transcriptional level (that is, the oxygen-dependent regulation of the HIF-1α) but also at the transcriptional and translational levels [39, 40]. In a region where the transcription and translation of HIF-1α increases, an excess amount of HIF-1α is likely to saturate the ubiquitin/proteasome degradation system and result in the upregulation of HIF-1, even under mildly hypoxic conditions. This may be one reason why the threshold of oxygen pressure for HIF-1 stabilization varies and depends upon the character of the organs or tumours. In such regions, the POS degradation rate would also decrease, because it contains the ODD domain and degrades in the same manner as HIF-1α. Thus, in imaging with POS-pretargeting and ^{123}I-IBB, it is possible to depict HIF-1-active regions that result from either hypoxic stabilization or the upregulation of transcription and translation.

Conclusion

Using the pretargeting method, clear tumour images were obtained in a shorter time than was possible with the direct-labelling method. Intratumoral accumulations of ^{125}I-IBB in the POS-pretargeted tumours were significantly correlated with HIF-1α-positive regions. These findings demonstrate that the pretargeting method with POS and ^{123}I-IBB is effective for the rapid imaging of HIF-1-active tumour hypoxia.

Acknowledgments The authors would like to thank Nihon Medi-Physics for providing ammonium ^{123}I-iodide. This work was supported in part by "R&D of Molecular Imaging Equipment for Malignant Tumor Therapy Support" of the New Energy and Industrial Technology Development Organization (NEDO), Japan, a Health Labour Sciences Research Grant for Research on Advanced Medical Technology from the Ministry of Health, Labour and Welfare of Japan, and a Grant-in-Aid for Exploratory Research (17659010) and a Grant-in-Aid for Young Scientists (B) (21791187) from the Ministry of Education, Culture, Sports, Science and Technology of Japan.

Conflicts of interest None.

References

1. Vaupel P, Kallinowski F, Okunieff P. Blood flow, oxygen and nutrient supply, and metabolic microenvironment of human tumors: a review. Cancer Res 1989;49:6449–65.
2. Semenza GL. Expression of hypoxia-inducible factor 1: mechanisms and consequences. Biochem Pharmacol 2000;59:47–53.
3. Wenger RH. Cellular adaptation to hypoxia: O2-sensing protein hydroxylases, hypoxia-inducible transcription factors, and O2-regulated gene expression. FASEB J 2002;16:1151–62.
4. Ballinger JR. Imaging hypoxia in tumors. Semin Nucl Med 2001;31:321–9.
5. Kizaka-Kondoh S, Inoue M, Harada H, Hiraoka M. Tumor hypoxia: a target for selective cancer therapy. Cancer Sci 2003;94:1021–8.

6. Jiang BH, Semenza GL, Bauer C, Marti HH. Hypoxia-inducible factor 1 levels vary exponentially over a physiologically relevant range of O2 tension. Am J Physiol 1996;271:C1172–80.
7. Harada H, Kizaka-Kondoh S, Li G, Itasaka S, Shibuya K, Inoue M, et al. Significance of HIF-1-active cells in angiogenesis and radioresistance. Oncogene 2007;26:7508–16.
8. Harada H, Kizaka-Kondoh S, Hiraoka M. Optical imaging of tumor hypoxia and evaluation of efficacy of a hypoxia-targeting drug in living animals. Mol Imaging 2005;4:182–93.
9. Kudo T, Ueda M, Kuge Y, Mukai T, Tanaka S, Masutani M, et al. Imaging of HIF-1-active tumor hypoxia using a protein effectively delivered to and specifically stabilized in HIF-1-active tumor cells. J Nucl Med 2009;50:942–9.
10. Kizaka-Kondoh S, Konse-Nagasawa H. Significance of nitroimidazole compounds and hypoxia-inducible factor-1 for imaging tumor hypoxia. Cancer Sci 2009;100:1366–73.
11. Kizaka-Kondoh S, Tanaka S, Harada H, Hiraoka M. The HIF-1-active microenvironment: an environmental target for cancer therapy. Adv Drug Deliv Rev 2009;61:623–32.
12. Green NM. Avidin. 3. The nature of the biotin-binding site. Biochem J 1963;89:599–609.
13. Goldenberg DM, Rossi EA, Sharkey RM, McBride WJ, Chang CH. Multifunctional antibodies by the Dock-and-Lock method for improved cancer imaging and therapy by pretargeting. J Nucl Med 2008;49:158–63.
14. Sharkey RM, Cardillo TM, Rossi EA, Chang CH, Karacay H, McBride WJ, et al. Signal amplification in molecular imaging by pretargeting a multivalent, bispecific antibody. Nat Med 2005;11:1250–5.
15. Sharkey RM, Karacay H, Litwin S, Rossi EA, McBride WJ, Chang CH, et al. Improved therapeutic results by pretargeted radioimmunotherapy of non-Hodgkin's lymphoma with a new recombinant, trivalent, anti-CD20, bispecific antibody. Cancer Res 2008;68:5282–90.
16. Kizaka-Kondoh S, Itasaka S, Zeng L, Tanaka S, Zhao T, Takahashi Y, et al. Selective killing of hypoxia-inducible factor-1-active cells improves survival in a mouse model of invasive and metastatic pancreatic cancer. Clin Cancer Res 2009;15:3433–41.
17. Foulon CF, Alston KL, Zalutsky MR. Synthesis and preliminary biological evaluation of (3-iodobenzoyl)norbiotinamide and ((5-iodo-3-pyridinyl)carbonyl)norbiotinamide: two radioiodinated biotin conjugates with improved stability. Bioconjug Chem 1997;8:179–86.
18. Motta-Hennessy C, Sharkey RM, Goldenberg DM. Metabolism of indium-111-labeled murine monoclonal antibody in tumor and normal tissue of the athymic mouse. J Nucl Med 1990;31:1510–9.
19. Ishino S, Kuge Y, Takai N, Tamaki N, Strauss HW, Blankenberg FG, et al. 99mTc-Annexin A5 for noninvasive characterization of atherosclerotic lesions: imaging and histological studies in myocardial infarction-prone Watanabe heritable hyperlipidemic rabbits. Eur J Nucl Med Mol Imaging 2007;34:889–99.
20. Ishino S, Mukai T, Kuge Y, Kume N, Ogawa M, Takai N, et al. Targeting of lectinlike oxidized low-density lipoprotein receptor 1 (LOX-1) with 99mTc-labeled anti-LOX-1 antibody: potential agent for imaging of vulnerable plaque. J Nucl Med 2008;49:1677–85.
21. Ueda M, Iida Y, Tominaga A, Yoneyama T, Ogawa M, Magata Y, et al. Nicotinic acetylcholine receptors expressed in the ventral posterolateral thalamic nucleus play an important role in anti-allodynic effects. Br J Pharmacol 2010;159:1201–10.
22. Harada H, Xie X, Itasaka S, Zeng L, Zhu Y, Morinibu A, et al. Diameter of tumor blood vessels is a good parameter to estimate HIF-1-active regions in solid tumors. Biochem Biophys Res Commun 2008;373:533–8.
23. Marignol L, Coffey M, Lawler M, Hollywood D. Hypoxia in prostate cancer: a powerful shield against tumour destruction? Cancer Treat Rev 2008;34:313–27.
24. Ke HL, Wei YC, Yang SF, Li CC, Wu DC, Huang CH, et al. Overexpression of hypoxia-inducible factor-1alpha predicts an unfavorable outcome in urothelial carcinoma of the upper urinary tract. Int J Urol 2008;15:200–5.
25. Miyake K, Yoshizumi T, Imura S, Sugimoto K, Batmunkh E, Kanemura H, et al. Expression of hypoxia-inducible factor-1alpha, histone deacetylase 1, and metastasis-associated protein 1 in pancreatic carcinoma: correlation with poor prognosis with possible regulation. Pancreas 2008;36:e1–9.
26. Trastour C, Benizri E, Ettore F, Ramaioli A, Chamorey E, Pouyssegur J, et al. HIF-1alpha and CA IX staining in invasive breast carcinomas: prognosis and treatment outcome. Int J Cancer 2007;120:1451–8.
27. Mees G, Dierckx R, Vangestel C, Van de Wiele C. Molecular imaging of hypoxia with radiolabelled agents. Eur J Nucl Med Mol Imaging 2009;36:1674–86.
28. Dunphy MP, Lewis JS. Radiopharmaceuticals in preclinical and clinical development for monitoring of therapy with PET. J Nucl Med 2009;50 Suppl 1:106S–21S.
29. Krohn KA, Link JM, Mason RP. Molecular imaging of hypoxia. J Nucl Med 2008;49 Suppl 2:129S–48S.
30. He F, Deng X, Wen B, Liu Y, Sun X, Xing L, et al. Noninvasive molecular imaging of hypoxia in human xenografts: comparing hypoxia-induced gene expression with endogenous and exogenous hypoxia markers. Cancer Res 2008;68:8597–606.
31. Yeom CJ, Chung JK, Kang JH, Jeon YH, Kim KI, Jin YN, et al. Visualization of hypoxia-inducible factor-1 transcriptional activation in C6 glioma using luciferase and sodium iodide symporter genes. J Nucl Med 2008;49:1489–97.
32. Sobhanifar S, Aquino-Parsons C, Stanbridge EJ, Olive P. Reduced expression of hypoxia-inducible factor-1alpha in perinecrotic regions of solid tumors. Cancer Res 2005;65:7259–66.
33. Li XF, Carlin S, Urano M, Russell J, Ling CC, O'Donoghue JA. Visualization of hypoxia in microscopic tumors by immunofluorescent microscopy. Cancer Res 2007;67:7646–53.
34. Serganova I, Doubrovin M, Vider J, Ponomarev V, Soghomonyan S, Beresten T, et al. Molecular imaging of temporal dynamics and spatial heterogeneity of hypoxia-inducible factor-1 signal transduction activity in tumors in living mice. Cancer Res 2004;64:6101–8.
35. Hsieh CH, Kuo JW, Lee YJ, Chang CW, Gelovani JG, Liu RS. Construction of mutant TKGFP for real-time imaging of temporal dynamics of HIF-1 signal transduction activity mediated by hypoxia and reoxygenation in tumors in living mice. J Nucl Med 2009;50:2049–57.
36. Wen B, Burgman P, Zanzonico P, O'Donoghue J, Cai S, Finn R, et al. A preclinical model for noninvasive imaging of hypoxia-induced gene expression; comparison with an exogenous marker of tumor hypoxia. Eur J Nucl Med Mol Imaging 2004;31:1530–8.
37. Ioannou M, Papamichali R, Kouvaras E, Mylonis I, Vageli D, Kerenidou T, et al. Hypoxia inducible factor-1 alpha and vascular endothelial growth factor in biopsies of small cell lung carcinoma. Lung 2009;187:321–9.
38. van den Broek GB, Wildeman M, Rasch CR, Armstrong N, Schuuring E, Begg AC, et al. Molecular markers predict outcome in squamous cell carcinoma of the head and neck after concomitant cisplatin-based chemoradiation. Int J Cancer 2009;124:2643–50.
39. North S, Moenner M, Bikfalvi A. Recent developments in the regulation of the angiogenic switch by cellular stress factors in tumors. Cancer Lett 2005;218:1–14.
40. Skinner HD, Zheng JZ, Fang J, Agani F, Jiang BH. Vascular endothelial growth factor transcriptional activation is mediated by hypoxia-inducible factor 1alpha, HDM2, and p70S6K1 in response to phosphatidylinositol 3-kinase/AKT signaling. J Biol Chem 2004;279:45643–51.

BJP BRITISH JOURNAL OF PHARMACOLOGY

BPS BRITISH PHARMACOLOGICAL SOCIETY

British Journal of Pharmacology (2010), 159, 1201–1210

0007-1188/10
www.brjpharmacol.org

RESEARCH PAPER

Nicotinic acetylcholine receptors expressed in the ventralposterolateral thalamic nucleus play an important role in anti-allodynic effects

M Ueda[1,2], Y Iida[3], A Tominaga[2], T Yoneyama[2], M Ogawa[4], Y Magata[4], H Nishimura[5], Y Kuge[2]* and H Saji[2]

[1]*Radioisotopes Research Laboratory, Kyoto University Hospital, Faculty of Medicine, Kyoto University, Kyoto, Japan,* [2]*Department of Patho-Functional Bioanalysis, Graduate School of Pharmaceutical Sciences, Kyoto University, Kyoto, Japan,* [3]*Bioimaging Information Analysis, Graduate School of Medicine, Gunma University, Maebashi, Japan,* [4]*Laboratory of Genome-Bio Photonics, Photon Medical Research Center, Hamamatsu University School of Medicine, Hamamatsu, Japan, and* [5]*Radioisotope Laboratory, Kyoto Prefectural University of Medicine, Kyoto, Japan*

Background and purpose: Much interest is currently being focused on the anti-nociceptive effects mediated by nicotinic acetylcholine (nACh) receptors, including their location and mechanism of action. The purpose of this study was to elucidate these issues using 5-iodo-3-(2(S)-azetidinylmethoxy)pyridine (5IA), a nACh receptor agonist, and [^{125}I]5IA.
Experimental approach: We partially ligated the sciatic nerve of Sprague-Dawley rat to induce neuropathic pain [Seltzer's partial sciatic nerve ligation (PSL) model]. We then examined the changes in nACh receptor density in the CNS using [^{125}I]5IA autoradiography and the involvement of nACh receptors in anti-nociceptive effects in the region where changes occurred.
Key results: Autoradiographic studies showed that the accumulation of [^{125}I]5IA and the number of nACh receptors in the thalamus of PSL rats were increased about twofold compared with those in the sham-operated rats. No change was observed in other brain regions. Rats injected in the ventral posterolateral thalamic nucleus (VPL) with 5IA demonstrated a significant and dose-dependent anti-allodynic effect and this effect was completely antagonized by mecamylamine, injected with 5IA, into the VPL. The blockade of nACh receptors in the VPL by mecamylamine decreased by 70% the anti-allodynic effect of 5IA, given i.c.v. Moreover, mecamylamine given intra-VPL by itself, induced significant hyperalgesia.
Conclusions and implications: Our findings suggest that the nACh receptors expressed in the VPL play an important role in the anti-allodynic effects produced by exogenous and endogenous agonists.
British Journal of Pharmacology (2010) **159,** 1201–1210; doi:10.1111/j.1476-5381.2009.00613.x; published online 5 February 2010

Keywords: nicotinic acetylcholine receptor; thalamus; ventral posterolateral thalamic nucleus; 5IA; anti-allodynic effect; neuropathic pain

Abbreviations: 5IA, 5-iodo-3-(2(S)-azetidinylmethoxy)pyridine; MPE, maximal possible effect; nACh, nicotinic acetylcholine; NRM, nucleus raphe magnus; PPTg, pedunculopontine tegmental nucleus; VPL, ventral posterolateral thalamic nucleus

Introduction

Numerous studies have shown that nicotinic acetylcholine (nACh) receptor agonists possess analgesic effects (Decker *et al.*, 2004; Jain, 2004). Because these effects are not antagonized by opioid receptor antagonists and arise from the activation of nACh receptors (Bannon *et al.*, 1998a; nomenclature follows Alexander *et al.*, 2008), much interest has been focused on nACh receptors as a novel target of anti-nociceptive drugs that do not involve the opioid system. Although morphine is a very well known and effective analgesic, its usefulness for patients with neuropathic pain is limited (Bannon *et al.*, 1998c; Sindrup and Jensen, 1999). In contrast, nACh receptor agonists are able to ameliorate neuropathic pain by affecting systems other than the opioids (Bannon *et al.*, 1998b,c; Decker *et al.*, 1998). Therefore,

Correspondence: Hideo Saji, Department of Patho-Functional Bioanalysis, Graduate School of Pharmaceutical Sciences, Kyoto University, 46-29 Yoshida Shimoadachi-cho, Sakyo-ku, Kyoto 606-8501, Japan. E-mail: hsaji@pharm.kyoto-u.ac.jp
*Present address: Central Institute of Isotope Science, Hokkaido University, Sapporo 060-0815, Japan.
Received 24 April 2009; revised 22 July 2009; accepted 18 October 2009

identification of the sites of action of nACh receptor agonists and the elucidation of their anti-allodynic mechanisms are desirable.

One of the most studied nACh receptor-acting analgesics is ABT-594. This compound is a selective and potent agonist with high affinity for α4β2-nACh receptors (predominant in the brain), low affinity for α7-nACh receptors and no affinity for α1β1γδ-nACh receptors (Donnelly-Roberts *et al.*, 1998; Holladay *et al.*, 1998). By virtue of this selectivity, ABT-594 has analgesic efficacy with an improved therapeutic window compared with non-selective agonists such as epibatidine (Bannon *et al.*, 1998b).

Recently, 5-iodo-3-(2(S)-azetidinylmethoxy)pyridine (5-iodo-A-85380, 5IA), an analogue of ABT-594, was synthesized (Saji *et al.*, 2002). It is also an α4β2-nACh receptor-specific agonist (Ueda *et al.*, 2008) with a relatively good safety profile (Vaupel *et al.*, 2003; Ueda *et al.*, 2004). In addition, radiolabelled 5IA, [$^{123/125}$I]5IA, was also developed (Saji *et al.*, 2002) and was reported to be a promising ligand for imaging nACh receptors in rodents and in humans (Saji *et al.*, 2002; Mamede *et al.*, 2004; Mamede *et al.*, 2007; Oishi *et al.*, 2007; Brasic *et al.*, 2009). Non-radioactive 5IA and [$^{123/125}$I]5IA can be considered the same compound with regard to their biodistribution or metabolism. Therefore, the pharmacokinetics, receptor occupancy and binding potential (an index of nACh receptor density) of 5IA are able to be measured readily using [$^{123/125}$I]5IA. Studies using 5IA have the advantage that pharmacodynamic effects can be compared directly with the pharmacokinetic profile of the compound.

Previous studies have demonstrated the up-regulation of spinal muscarinic acetylcholine receptors (Chen and Pan, 2003) and thalamic cannabinoid CB_1 receptors (Siegling *et al.*, 2001) in neuropathic pain models. It has been reported that the up-regulation of muscarinic and CB_1 receptors contributes to the increased analgesic efficacy of each agonist. As nACh receptor agonists are also effective against neuropathic pain, up-regulation of nACh receptors may also occur in such models. We hypothesized that brain regions where changes in the density or function of nACh receptors occurred would play an important role in anti-nociceptive effects, provided that such changes were found under neuropathic conditions. In the present study, we used a partial sciatic nerve ligation (PSL) model of neuropathic pain (Seltzer *et al.*, 1990) and examined the changes in nACh receptors in the PSL rats using [^{125}I]5IA. Furthermore, based on the result, we investigated the involvement of the nACh receptors expressed in the region where changes occurred as a result of the model of neuropathic pain.

Methods

Animals

Animal care and experimental procedures were conducted in accordance with our institutional guidelines, and the experimental procedures were approved by the Kyoto University Animal Care Committee.

Male Sprague-Dawley rats weighing 200–250 g were purchased from Japan SLC Co., Ltd. (Hamamatsu, Japan). The rats were kept at a constant ambient temperature under a 12 h light/dark cycle with free access to food and water.

Surgical operation

The PSL neuropathic pain model was established according to a previously published method (Seltzer *et al.*, 1990). Under sodium pentobarbital (50 mg·kg^{-1}, i.p.) anesthesia, the right sciatic nerve was exposed just distal to the branch leading to the posterior biceps femoris/semitendinosus muscles. A 7–0 silk suture was inserted into the nerve and tightly ligated so that the dorsal 1/3–1/2 of the nerve was trapped in the ligature. In the sham-operated rats, the sciatic nerve was exposed, but was left intact.

After recovery from the surgery, the rats were implanted with stainless steel guide cannulae (o.d. 0.7 mm, i.d. 0.38 mm) under sodium pentobarbital (50 mg·kg^{-1}, i.p.) anesthesia for i.c.v. or intra-ventral posterolateral thalamic nucleus (VPL) administration. The rats were placed into a stereotaxic apparatus (SR-5, Narishige Co., Ltd., Tokyo, Japan) and unilaterally implanted with a guide cannula above the lateral ventricle (0.8 mm posterior and 1.5 mm lateral to bregma, 2.0 mm below the outer surface of the skull) for i.c.v. administration or above the left VPL, which was contralateral to the nerve ligation (2.4 mm posterior and 3.3 mm lateral to bregma, 2.0 mm below the outer surface of the skull) for intra-VPL administration. The stereotaxic coordinates were determined following an atlas (Paxinos and Watson, 2005). The guide cannulae were held firmly in place using dental acrylic cement. After surgery, the rats were individually returned to their cages and left to recover for 5 days or more until the experiments.

von Frey filament test

Just before and 2 weeks after the PSL, tactile sensitivity was measured by the up-down method using calibrated von Frey filaments ranging from 0.07 to 26 g (North Coast Medical, Morgan Hill, CA, USA), in a previously described method with slight modifications (Marcil *et al.*, 2006). Briefly, for testing, the rats were individually placed on an elevated wire mesh floor. After a habituation period of 15–30 min, the tactile stimulus was applied to the middle plantar area of the each paw by placing the von Frey filament perpendicular to the surface of the paw. The filament was held in this position with enough force to cause slight bending. Each trial involved 10 applications of filaments every 1–2 s. The threshold was determined as the filament of the lowest stiffness at which the rat responded (quick paw flick) in one or more of the trial. The rats that showed a lower threshold postoperatively than preoperatively in both paws were considered as demonstrating allodynia and were used in the following studies.

Effect of 5IA and/or mecamylamine on tactile allodynia

For i.c.v. administration, an injection cannula (o.d. 0.35 mm, i.d. 0.18 mm) was inserted 5.0 mm below the surface of the skull along the guide cannula. Then, various concentrations of 5IA (1–10 nmol in 5 μL) or vehicle were infused at 5 μL per rat with a constant rate of 10 μL·min^{-1} using a microsyringe

pump (EP-60; Eicom Corporation, Kyoto, Japan). The cannula was retained in place for an additional 1 min to prevent backflow of the drugs. When required, mecamylamine (5 mg·kg^{-1}) was injected subcutaneously 30 min before i.c.v. administration of 5IA.

For intra-VPL administration, an injection cannula was inserted 6.2 mm below the surface of the skull. Subsequently, vehicle, 5IA (1–50 nmol in 0.5 μL), mecamylamine (1–10 nmol in 0.5 μL) or a mixed solution of 5IA and mecamylamine (10 nmol each in 0.5 μL) was infused at 0.5 μL per rat with a constant rate of 0.4 μL·min^{-1}. The cannula was retained in place for an additional 1 min.

For double injections, the cannula for intra-VPL administration was inserted intra-VPL, and mecamylamine (10 nmol in 0.5 μL) or vehicle was infused in the same way as described above. Five minutes later, the cannula for i.c.v. administration was inserted, and 5IA (10 nmol in 5 μL) or vehicle was infused as described above. Both cannulae were retained in place for an additional 1 min.

Just before and 15, 30, 60, 90 and 120 min after administration, tactile allodynia was evaluated using the von Frey filament test. The results were expressed as a percentage of the maximal possible effect (% MPE) according to the following formula:

$$\%\text{MPE} = \frac{\text{post-drug threshold} - \text{pre-drug threshold}}{\text{cut-off (26 g)} - \text{pre-drug threshold}} \times 100$$

Inclined plane test

The inclined plane test was carried out using a sliding apparatus (Medical Agent Co., Ltd., Kyoto, Japan), as described previously (Okada *et al.*, 2002). This procedure was used to evaluate the effects of anti-allodynic drugs on motor function (Fukui *et al.*, 2001; Okada *et al.*, 2002; Yasuda *et al.*, 2005). Intraperitoneal administration of baclofen, which causes muscle relaxation, significantly reduced the slope angle at which rats were no longer able to maintain their position and slid down the table, thus indicating the appropriateness of this procedure (Fukui *et al.*, 2001). Each rat was placed on a stainless steel plate inclined at 30°, and the angle of the plate was increased at a rate of 2°·s^{-1}. The maximum angle of the plane at which the rat maintained its body position without sliding down was determined.

The rats were habituated to the procedure three times per day. After 2 days of habituation, the test was performed three times, and the mean of the last two values was taken as a control. Soon after measuring the control value, drugs or vehicle were administered via each route, as described above, and the maximum angle before sliding down was determined at 15, 30, 60, 90 and 120 min after administration. Drugs were used at the maximum concentration for each administration route. The data are represented as a percentage of the control value.

Ex vivo *autoradiography*

Ex vivo autoradiography was performed using a previously described method (Kanegawa *et al.*, 2006) with slight modifications. Three groups of rats, a sham-operated group, a 2 week and a 1 month post-PSL group, were used in this experiment. Each group consisted of four to seven animals.

Each rat was injected with 2 MBq of [^{125}I]5IA via its tail vein and killed 60 min after radioligand injection. Their brains were quickly removed, frozen in hexane (–80°C) and cut into 20 μm-thick coronal sections with a cryomicrotome (CM3000, Leica, Germany). The sections were exposed to imaging plates (BAS-UR, Fuji Photo Film Co., Ltd., Tokyo, Japan) with ^{125}I autoradiographic microscale standards (Amersham Biosciences, Buckinghamshire, UK). After 25 h exposure, the [^{125}I]5IA autoradiograms were obtained using a bioimaging analyzer (BAS 3000, Fuji Photo Film Co., Ltd., Tokyo, Japan), and quantitative densitometric analyses were performed with dedicated software (Image Gauge ver. 3.1, Fuji Photo Film Co., Ltd., Tokyo, Japan). Regions of interest were drawn over eight brain regions bilaterally [frontal cortex, striatum, hippocampus, thalamus, pedunculopontine tegmental nucleus (PPTg), nucleus raphe magnus (NRM), locus coeruleus and cerebellum]. Data were represented as the mean of the ligated and contralateral side.

In vitro *autoradiography*

Three groups of rats were used as described for the *ex vivo* autoradiography. Each group consisted of five to seven animals. The rats were killed and their brains were removed and frozen immediately. Each frozen brain was cut into 20 μm-thick coronal sections, thaw-mounted onto gelatin-coated glass slides and kept frozen at –80°C until use.

A method for the autoradiographic determination of receptor density was previously published (Tanaka *et al.*, 1993; Suzdak *et al.*, 1994). A binding assay was conducted using a modification of a previously described method (Mukhin *et al.*, 2000). The assay buffer used was 50 mM Tris-HCl (pH 7.0) containing 120 mM NaCl, 5 mM KCl, 2.5 mM $CaCl_2$ and 1 mM $MgCl_2$. The sections were incubated with 23.75–380 pM [^{125}I]5IA (specific activity: 220 Ci·mmol^{-1}) in the same buffer for 1 h at 25°C, then rinsed twice in ice-cold buffer for 5 min each time, and once in distilled water for 1 min, and dried under a cold air stream. Non-specific binding was determined in the presence of 300 μM (–)-nicotine. The sections were exposed to the imaging plates with ^{125}I standards for 20 h. The autoradiograms were obtained and the quantitative analyses were performed in a similar way to that described above. Values for the maximum density of binding sites (B_{max}) were gained from saturation binding isotherms (one-site binding) of specific binding by means of nonlinear curve fitting (Prism 5.00, GraphPad Software, San Diego, CA, USA).

Statistical analyses

After the behavioural experiments, the rats were killed, and their brains were removed and frozen immediately. Coronal sections (20 μm) including the VPL were prepared and thaw-mounted onto gelatin-coated glass slides and subjected to Nissl staining. The placements of the tips of the injection cannulae were confirmed by using the atlas (Paxinos and Watson, 2005). Only data from rats with the injection cannulae correctly placed in the VPL were used for the statistical analyses.

The analyses of the data from the von Frey filament test and the inclined plane test were performed using two-way analysis of variance (ANOVA) with repeated measures. If there was a significant difference, a *post hoc* one-way ANOVA followed by a Tukey-Kramer multiple comparison test was performed using each treatment combination as an independent group. Analyses of the data from the autoradiographic studies were performed using a one-way ANOVA followed by a Tukey-Kramer multiple comparison test. Differences were considered significant when $P < 0.05$.

Materials

5IA and [^{125}I]5IA were synthesized according to a previously published method (Saji *et al.*, 2002). Mecamylamine hydrochloride, a nACh receptor antagonist, was purchased from Sigma-Aldrich (St. Louis, MO, USA). The sodium pentobarbital for injection was purchased from Dainippon Sumitomo Pharma Co., Ltd. (Osaka, Japan). All drugs were administered in physiological saline solution. All other chemicals used were of reagent grade.

Results

Anti-allodynic effect of i.c.v. administered 5IA

In the present study, the rats presented a bilateral tactile allodynia following the PSL. The paw withdrawal thresholds decreased from 13.4 ± 0.9 g to 3.1 ± 0.3 g and from 13.4 ± 1.0 g to 4.2 ± 0.4 g in the ligated paws and the contralateral paws respectively. First, we evaluated an anti-allodynic effect of i.c.v. administered 5IA, as there has been no previous report regarding whether 5IA is able to palliate neuropathic pain. Figure 1A shows the anti-allodynic effect observed in the ligated paws. Two-way ANOVA demonstrated significant main effects of treatment ($F_{3,90} = 5.56$, $P = 0.007$) and time ($F_{4,90} = 7.51$, $P < 0.001$) and a significant interaction between treatment and time ($F_{12,90} = 2.85$, $P = 0.003$). Injection of 5IA (10 nmol) increased % MPE values significantly at 15 min after administration (Vehicle: −3.4 ± 2, 10 nmol: 38 ± 6). Although the effect peaked at 15 min after administration and decreased gradually, significant increases in % MPE values were also observed in the 3 nmol- and 10 nmol-treated groups 30 min after administration. Similar results were also observed in the contralateral paws (data not shown).

Next, we examined an effect of mecamylamine, a blood–brain barrier permeable nACh receptor antagonist, on the anti-allodynic effect of 5IA. Significant main effects of treatment ($F_{3,95} = 6.75$, $P = 0.003$) and time ($F_{4,95} = 5.61$, $P < 0.001$) and a significant interaction between treatment and time ($F_{12,95} = 7.44$, $P < 0.001$) were found. Mecamylamine (5 mg·kg^{-1}, s.c.) blocked the effect of 5IA completely and the % MPE values were reduced to levels obtained after treatment with vehicle (Figure 1B).

Changes in the accumulation of [^{125}I]5IA in vivo

We compared [^{125}I]5IA accumulation between the PSL model rats and the sham-operated rats using an *ex vivo* autoradiographic method. Representative autoradiograms are shown in Figure 2A. The thalamic signals of the PSL groups were stronger than those of the sham-operated group, while the cortical and hippocampal signals were similar among the three groups. There was no difference between the ligated and contralateral sides of the PSL model rats. A significant increase (170%) in the accumulation of [^{125}I]5IA was observed only in the thalamus in both PSL groups and no detectable change was seen in other regions (Figure 2B).

Measurement of the density of nACh receptors in vitro

We performed an autoradiographic saturation assay using [^{125}I]5IA as a radioligand. The saturation binding curves are

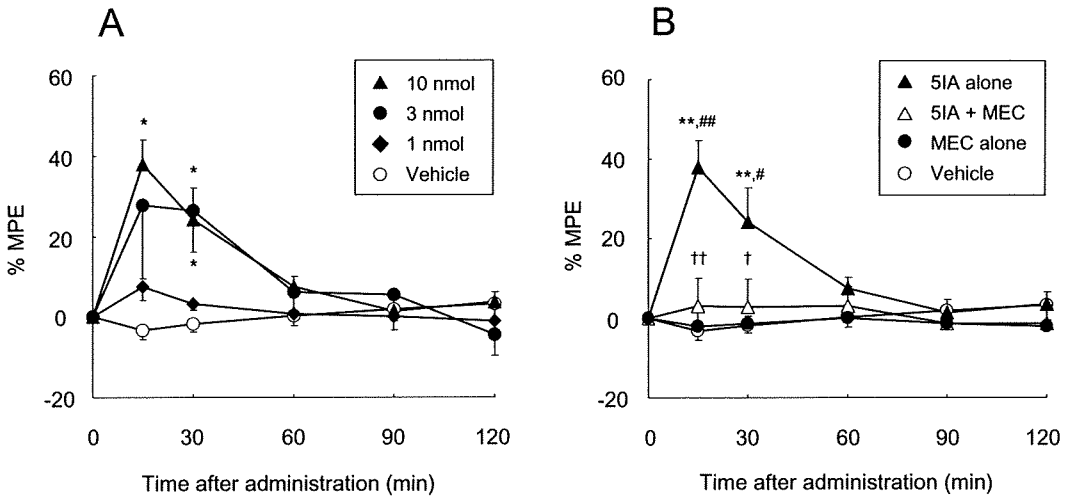

Figure 1 (A) Effect of i.c.v. administered 5IA on neuropathic tactile allodynia. Data are presented as a percentage of the maximum possible effect (% MPE). Each point represents the mean ± SEM of the ligated paws of five to six animals per group. *$P < 0.05$ versus vehicle at the same time point. (B) Effect of mecamylamine (MEC, 5 mg·kg^{-1}, s.c., 30 min prior) on the anti-allodynic effect induced by 5IA (i.c.v.). Data are presented as a percentage of the maximum possible effect. Each point represents the mean ± SEM of the ligated paws of five to six animals per group. **$P < 0.01$ versus vehicle, #$P < 0.05$, ##$P < 0.01$ versus MEC alone, and †$P < 0.05$, ††$P < 0.01$ versus 5IA alone at the same time point. 5IA, 5-iodo-3-(2(S)-azetidinylmethoxy)pyridine; MPE, maximal possible effect.

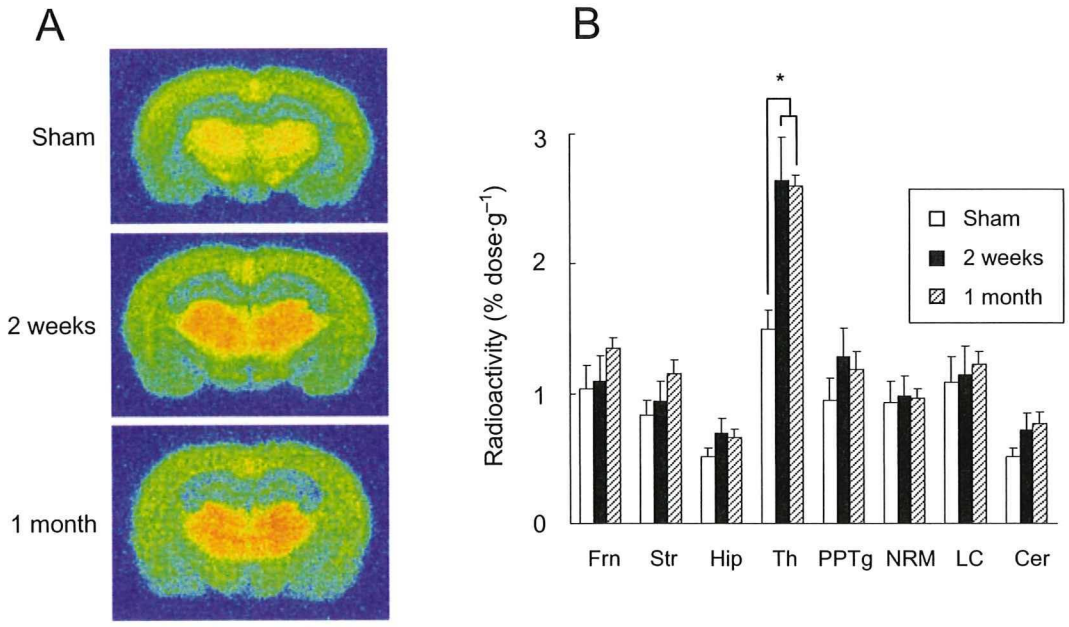

Figure 2 (A) Representative autoradiograms of brain regions from sham-operated and PSL rats given [^{125}I]5IA, i.v. (B) Changes in the regional accumulation of [^{125}I]5IA in Seltzer's PSL model of neuropathic pain. A significant increase was observed only in the thalamus, and no detectable change occurred in other regions. Each column represents the mean ± SEM of four to seven animals per group. *$P < 0.05$ versus sham. PSL, partial sciatic nerve ligation; 5IA, 5-iodo-3-(2(S)-azetidinylmethoxy)pyridine; Frn, frontal cortex; Str, striatum; Hip, hippocampus; Th, thalamus; PPTg, pedunculopontine tegmental nucleus; NRM, nucleus raphe magnus; LC, locus coeruleus; Cer, cerebellum.

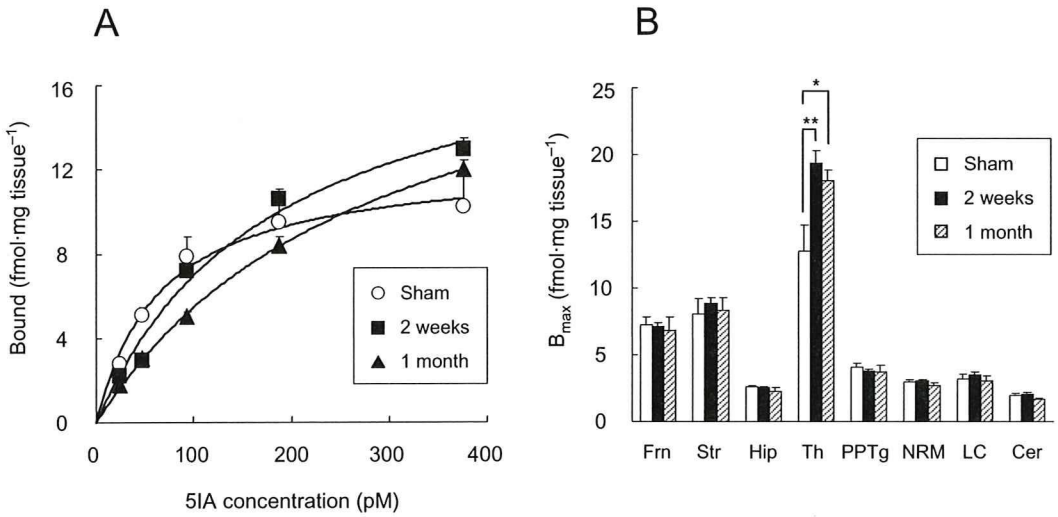

Figure 3 (A) Saturation curves of [^{125}I]5IA binding to sham-operated and PSL rat thalamus determined *ex vivo*. Each point represents the mean ± SEM of five to seven animals per group. The B_{max} values estimated by nonlinear regression analysis of these mean data were 12.5, 19.9 and 21.2 fmol/mg protein in sham-operated, 2 week post-PSL, and 1 month post-PSL group respectively. (B) Changes in nACh receptor density in brain regions of rats with Seltzer's PSL model of neuropathic pain. A significant increase was observed only in the thalamus, and no detectable change occurred in other regions. Each column represents the mean ± SEM of five to seven animals per group. *$P < 0.05$, **$P < 0.01$ versus sham. PSL, partial sciatic nerve ligation; 5IA, 5-iodo-3-(2(S)-azetidinylmethoxy)pyridine; Frn, frontal cortex; Str, striatum; Hip, hippocampus; Th, thalamus; PPTg, pedunculopontine tegmental nucleus; NRM, nucleus raphe magnus; LC, locus coeruleus; Cer, cerebellum.

presented in Figure 3A. As with the *ex vivo* autoradiography, both PSL groups showed a significant increase in B_{max} value that occurred in the thalamus only (Figure 3B). The percentage increase in B_{max} values in the thalamus (150%) was similar to those observed in the *ex vivo* autoradiographic findings.

Anti-allodynic effect of 5IA given intra-VPL

Based on previous reports (Kupers and Gybels, 1993; Derbyshire *et al.*, 1997; Gybels, 2001), we predicted that the VPL was involved in the expression of anti-nociceptive effects and investigated the association between nACh receptors expressed in the VPL and the anti-allodynic effect of 5IA.

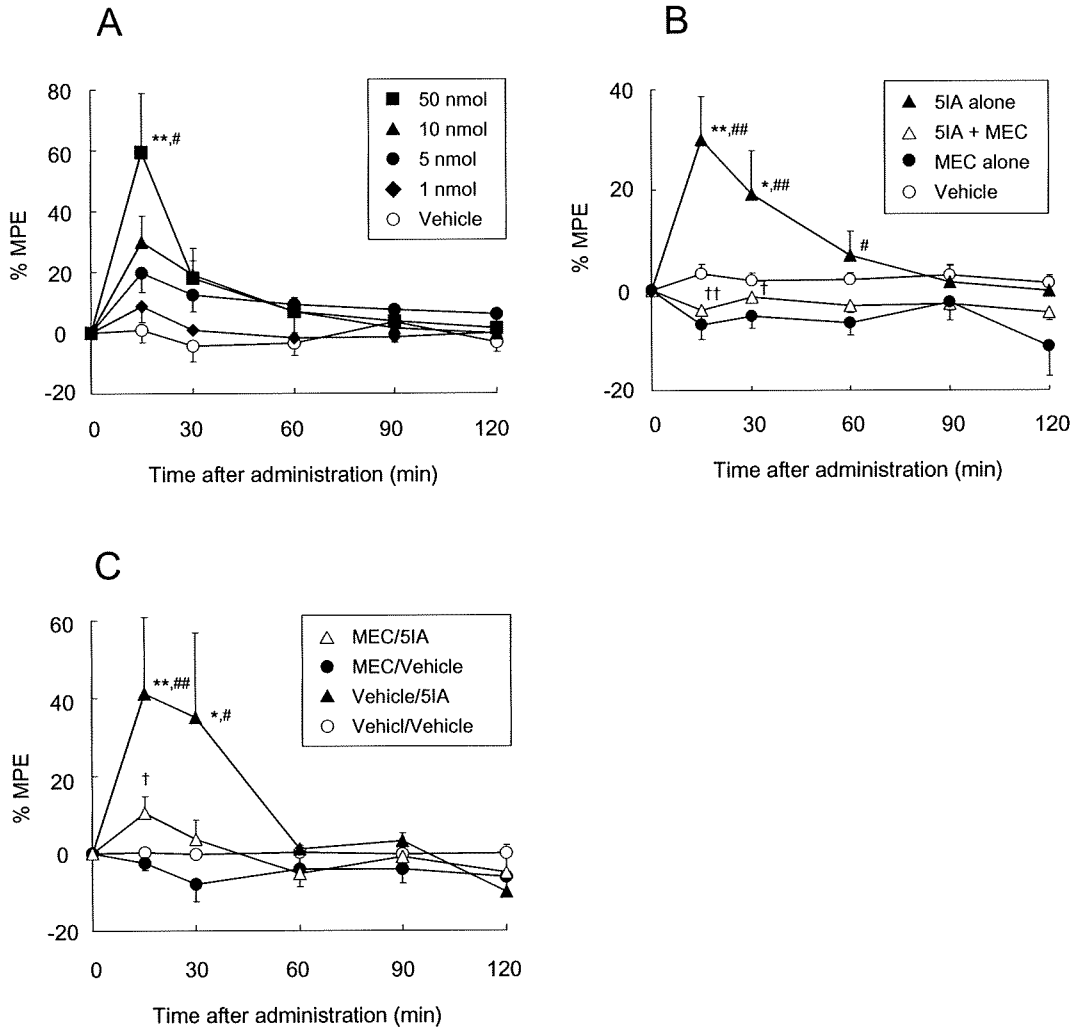

Figure 4 (A) Effect of 5IA injected intra-VPL on neuropathic tactile allodynia. Data are presented as a percentage of the maximum possible effect (% MPE). Each point represents the mean ± SEM of the ligated paws of five to six animals per group. *$P < 0.05$, **$P < 0.01$ versus vehicle, and #$P < 0.05$ versus 1 nmol of 5IA at the same time point. (B) Effect of mecamylamine (MEC, 10 nmol in 0.5 μL) administered concurrently with 5IA in an intra-VPL manner on the anti-allodynic effect produced by 5IA (10 nmol in 0.5 μL, intra-VPL). Data are presented as a percentage of the maximum possible effect. Each point represents the mean ± SEM of the ligated paws of five to six animals per group. *$P < 0.05$, **$P < 0.01$ versus vehicle, #$P < 0.05$, ##$P < 0.01$ versus MEC alone, and †$P < 0.05$, ††$P < 0.01$ versus 5IA alone at the same time point. (C) Effect of mecamylamine (MEC, 10 nmol in 0.5 μL, intra-VPL, 5 min prior) on the anti-allodynic effect produced by 5IA (10 nmol in 5 μL, i.c.v.). Data are presented as a percentage of the maximum possible effect. Each point represents the mean ± SEM of the ligated paws of four to seven animals per group. *$P < 0.05$, **$P < 0.01$ versus vehicle/vehicle, #$P < 0.05$, ##$P < 0.01$ versus MEC/vehicle, and †$P < 0.05$ versus vehicle/5IA at the same time point. 5IA, 5-iodo-3-(2(S)-azetidinylmethoxy)pyridine; MPE, maximal possible effect; VPL, ventral posterolateral thalamic nucleus.

Figure 4A shows the anti-allodynic effects that occurred in the ligated paws of rats that received 5IA intra-VPL. Two-way ANOVA demonstrated significant main effects of treatment ($F_{4,115} = 3.97$, $P = 0.014$) and time ($F_{4,115} = 13.6$, $P < 0.001$) and a significant interaction between treatment and time ($F_{16,115} = 3.11$, $P < 0.001$). There was a significant difference between the 50 nmol-treated group and the vehicle- or 1 nmol-treated groups. Although one-way ANOVA revealed a significant difference between the data at 30 min after administration ($P = 0.028$), the *post hoc* Tukey test showed no significant difference.

Subsequently, we injected a mixed solution of 5IA and mecamylamine (10 nmol each) intra-VPL and performed the von Frey filament test. Two-way ANOVA demonstrated significant main effects of treatment ($F_{3,85} = 11.34$, $P < 0.001$) and time ($F_{4,85} = 5.22$, $P = 0.001$) and a significant interaction between treatment and time ($F_{12,85} = 4.05$, $P < 0.001$). Mecamylamine antagonized the 5IA-induced anti-allodynic effect completely, and furthermore, the % MPE values of mecamylamine-treated rats tended to decrease compared with those of the vehicle-treated rats, although the difference was not significant (Figure 4B).

Involvement of nACh receptors in the VPL in the anti-allodynic effect induced by i.c.v. 5IA administration

To explore to what extent nACh receptors in the VPL were involved in the anti-allodynic effects arising from central